Current-perpendicular and current-parallel giant magnetoresistances in Co/Ag multilayers

S.-F. Lee,* Q. Yang, P. Holody, R. Loloee, J. H. Hetherington, S. Mahmood,† B. Ikegami, K. Vigen, L. L. Henry,
P. A. Schroeder, W. P. Pratt, Jr., and J. Bass‡

*Department of Physics and Astronomy and Center for Fundamental Materials Research, Michigan State University,
East Lansing, Michigan 48824-1116*

(Received 25 May 1995; revised manuscript received 27 July 1995)

We report results of measurements of the perpendicular [current perpendicular to the layer planes (CPP)] and parallel [current in the layer planes (CIP)] magnetoresistances (MRs) of Co/Ag multilayers having Co and Ag thicknesses t_{Co} and t_{Ag} ranging from 1.5 to 60 nm. (1) We find the variations of the CPP- and CIP-MRs with t_{Ag} and t_{Co} to be qualitatively similar to each other, suggesting that the parameters determining both may also be similar. (2) In accord with predictions that CPP-MR>CIP-MR, we find their ratio π=CPP-MR/CIP-MR to range from about 3 to at least 6. (3) We analyze current perpendicular to the layer plane (CPP) specific resistances, $A r_t$, of Co/Ag multilayers having a wide range of Co and Ag thicknesses t_{Co} and t_{Ag} in terms of a two-current, series resistor model based upon the assumption that the spin-diffusion lengths in the Co and Ag are much longer than t_{Co} and t_{Ag}, respectively. We show first that a six parameter fit gives rather good agreement with four data sets, with the three parameters that can be separately checked agreeing within experimental uncertainties with independent measurements of the same quantities. We then examine the ability of these fits to predict the behavior of additional sets of data. Here we find some agreements and some disagreements. Possible reasons for the disagreements are examined.

I. INTRODUCTION

Giant (G) negative magnetoresistance (MR) in magnetic multilayers composed of alternating layers of a ferromagnetic (F) metal and a nonmagnetic (N) metal is now a topic of great interest for both scientific and technological reasons.[1,2] Most GMR measurements are made with the current in the layer planes (CIP-MR),[2,3] because this geometry leads to resistances $\geq 10^{-2} \Omega$, which are easy to measure and large enough for use in devices. The CPP-MR, in contrast, is harder to measure. A 1 μm thick sample of typical CIP area $A \approx 1$ cm $\times 1$ mm$\approx 10^{-5}$ m^2 has a CPP resistance $R \sim 10^{-8} \Omega$, which poses an experimental challenge.[4] Alternatively, complex lithography can be used to reduce the sample area to $A \sim 10^{-10}$ m^2, increasing the CPP resistance to an easily measured $R \sim 10^{-3} \Omega$ but, so far, at the cost of a nonuniform current in the sample.[5] We and others have argued, however, that the GMR with the current perpendicular to the layer planes (CPP-MR) has two important advantages that make it important to measure. (1) As predicted by Zhang and Levy,[6] the CPP-MR is expected to be several times larger than the CIP-MR. (2) As suggested by Zhang and Levy,[6] demonstrated experimentally by us,[7] and subsequently confirmed from more rigorous analysis by Valet and Fert[8] and others,[9] it is usually easier in the CPP-MR to separate effects of electron scattering in bulk F metal from those at F/N interfaces. In this paper we examine issues (1) and (2) using Co/Ag as a test system. We chose Co/Ag on the recommendation of Schuller, for two reasons: (a) sputtered Co/Ag multilayers had shown strong high angle x-ray satellites;[10] (b) Co and Ag are immiscible,[11] so there should be minimal intermixing at Co/Ag interfaces.

The fundamental quantity in the CPP geometry is the conductance per unit area, or its inverse, $A R_t$, the sample area A times its total resistance, R_t (see Fig. 1). Since the CIP and CPP resistances are so different in size, they are compared using the normalized percentage magnetoresistance:

$$\text{MR}(H) = 100[R(H) - R(H_s)]/R(H_s), \quad (1)$$

where H_S is the saturation magnetic field at which $R(H)$ reaches its minimum value.

(1) Comparison of CPP- and CIP-MRs. So far, comparisons of CPP and CIP data for samples with the same F and N metals, and the same values of t_F and t_N, have been published for only relatively few samples: two series of Co/Ag,[4] two series of Co/Cu,[5,12] and one series of Fe/Cr.[5] To fully test their models, theorists need more complete data on a single system. In Sec. III, we present CPP-MR and CIP-MR data for seven different series of Co/Ag data. We first examine the variations of the CPP- and CIP-MRs with t_{Ag}, t_{Co}, or both at once. We then examine the values of, and variations in, their ratio π=CPP-MR/CIP-MR.

(2) Quantitative analysis of CPP-AR. It is difficult to isolate the fundamental physical parameters underlying GMR from the CIP-MR, because it varies in an essential way with
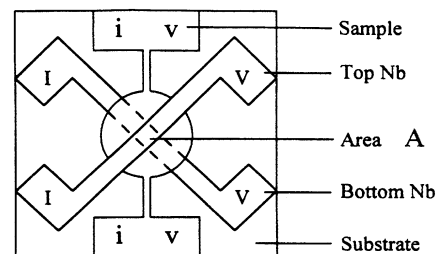

FIG. 1. Sample shape. The perpendicular (CPP) resistance, $R = V/I$, is measured only over the area A of the overlap of the crossed Nb strips. The parallel (CIP) resistance, $R = v/i$, is dominated by the contributions from the two narrow strips.

the ratios t_N/λ_p^N and t_F/λ_p^F, where λ_p^N and λ_p^F, are the mean-free paths in the N and F metals.[2] In contrast, in the limit of long spin diffusion lengths, l_{sf}^{Ag} and l_{sf}^{Co}, that is expected to apply to our Co/Ag multilayers at our measuring temperature of 4.2 K,[8] the CPP-MR is independent of these mean-free paths, and should be well described by a simple two current model that allows straightforward determinations of the fundamental parameters in both the bulk F metal and at the F/N interfaces.[6–8] In Sec. IV, we describe this model, its conditions of validity, and its limitations. We have previously demonstrated its ability to simultaneously fit three series of Co/Ag multilayers with one assumed parameter,[7] three series of Co/Cu multilayers with one assumed parameter,[12] and two series of NiFe/Cu multilayers with two assumed parameters.[12] In Sec. V, we test this model more stringently by investigating first, how well it can fit data for four series of Co/Ag multilayers with no assumed parameters, and then how well the parameters derived from these four series describe data for three new series of multilayers.

The paper is organized as follows. In Sec. II, we describe our sample making techniques, sample characterization, and measuring uncertainties, with particular emphasis on a mask changing system. In Sec. III, we present and discuss our CPP- and CIP-MR data, and examine the ratio π. We describe the theory underlying our quantitative CPP analysis in Sec. IV, and the analysis in Sec. V. In Sec. VI, we summarize our results and present our conclusions.

II. SAMPLE PREPARATION, SAMPLE CHARACTERIZATION, AND MEASURING UNCERTAINTIES

A. Experimental techniques and procedures

As our basic technique for dc sputtering multilayers for simultaneous CPP-MR and CIP-MR measurements has already been described,[4,13] we focus here mainly on procedures specific to the present measurements and on modifications to previously described ones. The most important modification is a mask changing system. Other details are given elsewhere.[14]

To obtain comparable sample quality for different Co and Ag layer thicknesses, we held sputtering conditions as nearly constant as possible. The sputtering system was initially pumped down to $\leq 2 \times 10^{-8}$ Torr, high purity Ar sputtering gas was admitted to a pressure of 2.5 mTorr, and the substrates were held at temperatures between $-30\,^\circ\text{C}$ and $+30\,^\circ\text{C}$ using a substrate cooling system.[15] Although the sputtering voltages and currents were held within narrow ranges, we found some variations in sputtering rates in targets bought from different manufacturers over several years, and also as targets thinned. The samples described in this paper were made with rates within the ranges: $\approx 1.1-1.4$ nm/s for Ag, $\approx 0.8-1.0$ nm/s for Co, and $\approx 0.90-1.0$ nm/s for Nb.

The substrates are mostly polished, 0.5″ square, c-axis oriented, single crystal sapphire, cleaned in acetone, and then given a final ultrasonic rinse in alcohol. To check that the substrate material is not crucial to our results, a few samples were sputtered onto (100) single crystal silicon, and a few CIP samples were sputtered also onto thin Nb films deposited
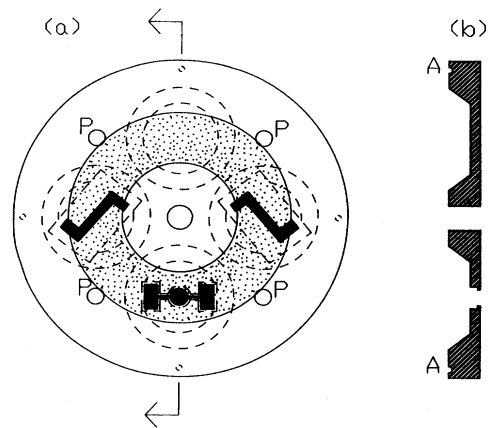

FIG. 2. The mask plate. (a) The mask plate as seen from the substrate side. (b) Cross section through the center of the mask plate. The mask holes (shown as black) are separated from the substrate by a 25.4 μm deep circular depression, shown dotted. Each mask hole is countersunk to allow maximum flux through the hole. The four rods for rotating the substrate go into the four holes P located on a square. The small circular holes labeled A are used to set the mask placement, as shown in Fig. 3.

on Si. Since the results for the various alternatives are not very different,[14] we describe only data on sapphire.

An *in-situ* mask changing system in the sputtering chamber lets us fabricate the sample shape shown in Fig. 1 to allow simultaneous CPP and CIP resistance measurements on different parts of the sample. The substrates are held in an actively cooled, circular aluminum sample-positioning plate (SPP) described elsewhere[13] that is located about 12 cm above the guns. Each of the eight circular holes in the SPP can hold either a single substrate plus masks for making a CPP/CIP sample, or two substrates for making thin films or simple CIP multilayers. Two other holes allow quartz crystal thickness monitors to measure deposition rates at the locations of the substrates. The SPP oscillates under computer control to bring the substrate of interest sequentially over the desired targets for chosen amounts of time. All of the samples in this study were made with a mask changing system that we now describe.

The masking system components are shown in Figs. 2 and 3. Figure 2(a) shows the 3 mm thick, 64 mm diam., stainless steel mask plate as seen from the substrate side, and Fig. 2(b) shows a cross section through the center of the mask plate. The mask plate contains four masks that are changed sequentially by pulling upon small cylindrical posts (screwed into the four holes labeled P), using a wobble stick that extends outside the chamber. The holes in the masks are shown as black. One mask is blank, to close off the substrate from unwanted material. The first sputtering mask is its clockwise neighbor, which contains a 1 cm long, $W=1$ mm wide strip (with contact pads), through which a 500 nm (or, more recently, 300 nm) thick, Nb strip is sputtered directly onto the substrate. The multilayer mask is then pulled into place and the multilayer is sputtered. The last mask, with a 1 cm long, $W=1$ mm wide strip perpendicular to the first one, is then pulled into place and a Nb cross strip is sputtered. Finally, the blank mask is pulled back over the substrate to protect it
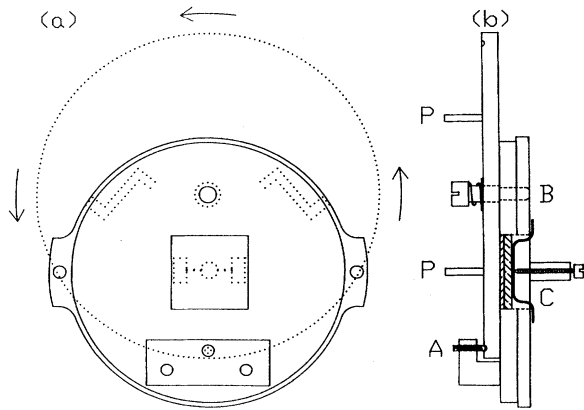
FIG. 3. (a) Composite showing the essential features of the circular substrate holder (solid figure) with the mask plate (dotted figure) in its offset orientation so that each mask hole (or the blank) can be rotated directly over the substrate. The substrate is centered in a square hole in the substrate holder so that it rotates directly over the center of each sputtering target. (b) Side view showing the substrate holder, the mask plate (now also solid), the slip-fit cylindrical piece ending in a screw (B) that presses the mask plate against the substrate holder, and (in cutaway view labeled C) the set-screw pushing on a copper plate (hatched) that presses the substrate (oppositely hatched) against the mask plate. A copper band (shown rotated by 90° from its actual position) is hard soldered to the copper plate and screwed (not shown) into the substrate holder to make good thermal contact. At A, a spring loaded ball slips into one of the four circular holes shown in Fig. 2 when the appropriate mask is properly aligned.

FIG. 4. Dektak profile of a Nb strip. The vertical scale is in Å, the horizontal scale in μm, giving a 2×10^3 difference between the two scales.

until it is removed from the system. The mask holes are cut using "sinker" spark erosion. Around these holes, the mask plate is countersunk by spark erosion to a thickness ≤ 0.25 mm to allow maximum flux of sputtered material onto the substrate and to minimize reflection of sputtered atoms off the hole edges onto the substrate. The countersunk area around each Nb hole is a large rectangle, while that around the multilayer hole follows the shape of the hole. To protect the sample as the mask plate rotates over it, the surface of the mask plate is cut back by $0.001''$ (25.4 μm) to form a ring-shaped depression [dotted area in Fig. 2(a)] directly over the masks. Outside of this depression, the mask plate makes direct contact with the substrate and its holder (described next), thus keeping the mask-to-substrate distance constant for all masks.

The substrate sits in the middle of a circular, aluminum substrate holder that is mounted in any of the eight holes in the SPP.[13] Figure 3(a) shows the substrate holder with a "ghost" overlay of the mask holes in the offset mask plate showing how the masks rotate into place over the substrate. Figure 3(b) shows a side view of the substrate holder, the mask plate, and the piece used to lock them together, with a cutaway view of the screw used to hold the substrate against a 2.5 mm thick copper backing plate, to which is hard soldered a 0.4 mm thick, 5 mm wide, copper strip (shown rotated 90° to its actual position) that is screwed to the substrate holder to provide thermal coupling. The substrate holder is then thermally anchored to the actively cooled SPP.
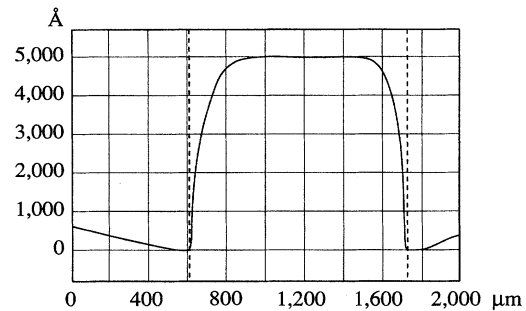
The system is assembled by first loading the substrate holder into one of the holes in the SPP, and then attaching the mask plate.

Even though the mask holes lie within 25 μm of the substrate, the large angular spread of sputtered atoms gives substantial shadowing around the mask edges, e.g., sputtering through the 1 mm wide slots typically yields Nb strips ≈ 1.1 mm wide, and sputtering through the 0.3 mm wide thinnest CIP parts of the mask gives ≈ 0.4 mm wide sample strips. Figure 4 shows a Dektac profilometer scan across a typical Nb strip. The Nb edges have a small slope, only about 0.5% in the case shown. The importance of this slope for our measurements is discussed in the Appendix.

For the samples described in this paper, we used two sputtering procedures that differed in the time between sputtering of the first Nb strip and the multilayer. Since we found no systematic differences between data with the two procedures, we do not distinguish the two cases here and refer the reader to Ref. 14 for further details.

The CIP resistance $R = v/i$ is measured by passing current i from one pad to the other in Fig. 1, and measuring the resulting voltage v with a conductance bridge or digital voltmeter. R is dominated by the two narrow strips in Fig. 1. The intrinsic CIP quantity is the average resistivity, $\rho = RA/2l$, where l is the length of each strip and A is its cross-sectional area.

The CPP resistance R_t is measured by passing $I = 50$ mA into one Nb strip and taking it out of the other, using a bridge circuit[16] with a superconducting quantum interference device null detector to balance the voltage difference V between the strips against that produced by a balancing current, I_b, passing through a known (1.84 ± 0.02 $\mu\Omega$) reference resistance R_r. The measured ratio, $c = I_b/I$, then gives $R_t = (I_b/I)R_r$. Checks are routinely made for current independence, and rare samples that show any dependence are rejected.

At our measuring temperature of 4.2 K, the two Nb strips superconduct, thereby causing the current to bypass those parts of the multilayer outside their overlap area $A = W^2$, and pass only through that part of the multilayer within A. In the Appendix we show that this statement is correct to terms of order $t_T/W \approx 10^{-3}$, where t_T is the multilayer thickness. We determine A by measuring the width W of each Nb strip with a Dektac surface profilometer. Based upon independent measurements showing that Nb strips in contact with Co remain superconducting down to thicknesses of about 10 nm, we

define the edge of the profile in Fig. 4 to be where the Nb thickness is ≈ 10 nm. The bottom layer of the multilayer is always Co and in most samples t_T is held as close as possible to 720 nm, consistent with an integer number of bilayers. Some of the later multilayers are capped with a last Co layer, but most of those presented in this study are not. If not, the Ag layer touching the top Nb strip should become superconducting due to the proximity effect,[17] but the resistance of a single Ag layer is within our measuring uncertainty.

B. Sample characteristics and quality

We check our bilayer thicknesses, Λ, and the structure of our multilayers, with low angle and high angle θ-2θ x-ray scans. The high angle scans show peaks for the close packed planes of Ag, Co, and Nb, plus multilayer satellites. Our data thus confirm the usual experience that sputtered Co/Ag multilayers are highly textured, with the close-packed planes lying in the layers. The high angle line widths imply typical coherence lengths of 20–40 nm perpendicular to the layer planes. Our CPP/CIP samples on sapphire typically give few if any low angle satellites, a lack we attribute to a combination of curvature of the polished sapphire substrates, plus the columnar growth often found in sputtered samples. As listed in detail elsewhere,[14] both the mean and median of the x-ray derived bilayer thicknesses were about 4% less than the intended thicknesses.

The total thicknesses t_T of several nominally 720 nm thick samples were checked with a Dektac sample profilometer, and found to be within 5% of the intended values.[14]

Cross-sectional TEM[18] measurements of Co/Ag samples prepared in our sputtering system show that after a few uniform layers, columnar growth begins, with column widths $\sim$20–40 nm. The individual layers are polycrystalline, with crystallite sizes determined by the column width. Within each column, the layering is usually rather good, but the layers in neighboring columns are not always in registry. NMR studies[19] show that our Co/Ag interfaces are rather sharp, but incoherent, i.e., the Co and Ag have different in-plane lattice parameters.

Measuring Uncertainties and Reproducibility. The uncertainty in the CIP resistance, $R=v/i$, arises from the uncertainties in v and i, each of which is measured with a sensitivity of parts in 10^4 and an absolute accuracy of about 1%. The main uncertainties in $\rho=RA/2l$ are geometrical, with the largest uncertainty being in the cross-sectional area A of the narrow strips in Fig. 1, for two reasons: (1) Sputtering through the multilayer mask of Fig. 2 gives feathered rather than sharp sample edges, which complicates measurements of both the thicknesses and widths of the thin strips that dominate the CIP resistance. (2) The combination of oscillation of the substrates over the Co and Ag targets, with substrate inertia, can lead to only partial overlap of the Co and Ag layers. Initially, the square sapphire substrates fit snugly into their holders. But repeated cleaning with acid gradually expands the holders until the substrates can shift slightly when the holder stops over a target, if the substrates are not locked tightly into place. The process of tightening involves balancing the possibility of such a shift against that of too much friction between the mask plate and the substrate holder or even breaking the brittle substrate. Substrate shifts offset the Co and Ag layers from each other along the narrow
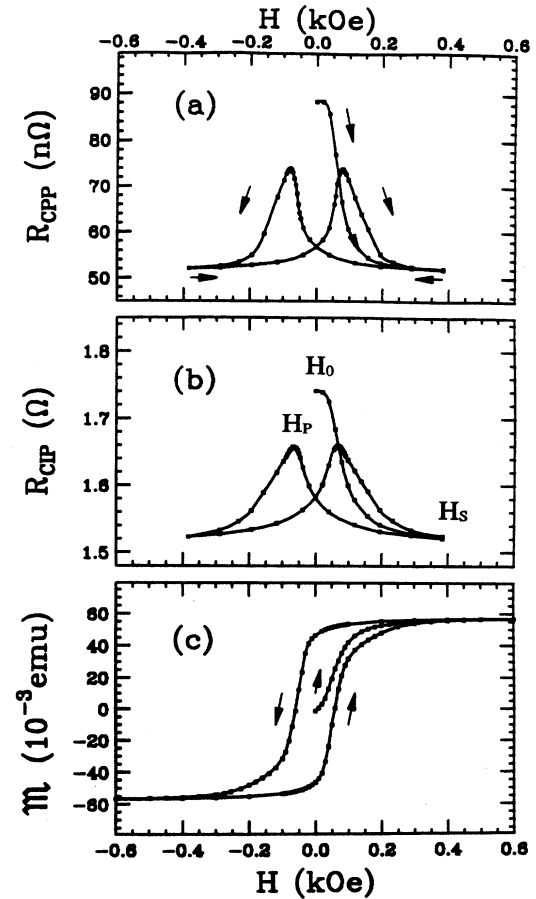

FIG. 5. (a) CPP-$R(H)$ and (b) CIP-$R(H)$ for a Co/Ag (6 nm/6 nm)$_{60}$ multilayer, and (c) magnetization, $\mathcal{M}(H)$ for a similar multilayer. The different CPP and CIP peak locations are due to slightly different fields at the CPP and CIP portions of the sample (see text).

strips, usually leading to a smaller CIP-MR. Sometimes an offset can be seen immediately, but other times it becomes clear only after the samples sit for some weeks and oxidize. In this paper we present only CIP data where the offsets are small (thus omitting some data points previously published[4]). The complete data are given elsewhere.[14]

Fortunately, substrate inertia should not affect the CPP-AR_t, as the Nb strips cross over the middle of the sample. The largest uncertainty in R_t is the 1% uncertainty in the reference resistor. Except for an occasional sample with a particularly small $R_t < 10^{-8}$ Ω, the uncertainty in AR_t is dominated by the uncertainty in $A = W^2$, where the width W of each Nb strip is measured with a surface profilometer (see the Appendix). The resulting uncertainty in A usually ranges from 2–5 %. Since our data actually vary by somewhat more than 2–5 %, there must be some variations in the physical and/or magnetic structures of individual samples. Attempts to better characterize these structures are underway.

Typical magnetic field dependences of the CPP-$R(H)$, CIP-$R(H)$, and magnetization $\mathcal{M}(H)$ of our samples are illustrated in Fig. 5. For both CPP and CIP geometries, $R(H)$ is usually largest in the as-prepared state, which we designate

$R(H_o)$. It then decreases with increasing field until it reaches a minimum value above a saturation field H_s, after which it cycles reproducibly with field with subsequent maxima $R(H_p)$ at a field H_p. The remnant magnetization is typically about 80% of the saturation magnetization.

Most investigators use $R(H_p)$ to calculate the CIP- and CIP-MRs of Eq. (1), mainly because it is reproducible; i.e., the same value is obtained upon repeated cycling to above H_s, even after heating to room temperature and recooling. To allow our data to be compared with data from other groups, we must thus present it at H_p. We, however, have argued (see Refs. 4, 12, 20, and Sec. IV below) that, for most of our samples, the nonreproducible $R(H_o)$ is a better approximation to the resistance of the antiparallel (AP) state, state with magnetizations M_i of adjacent layers antiparallel to each other, that is assumed in most theoretical analyses. For completeness, we thus present all of our CPP and CIP results in this paper at both H_o and H_p.

In Fig. 5, H_p(CPP) is a little larger than H_p(CIP), and both are slightly larger than the coercive field, H_c, where $\mathcal{M}(H)=0$. The different values of H_p appear to be an artifact of nonuniformity of the small magnet used in the present measurements, leading to slightly different fields at the CPP and CIP parts of the sample. Measurements using a system with a more uniform magnet show identical H_p values for CIP and CPP to within the measuring uncertainty of a few Oersteds. On the other hand, independent checks show that H_c does appear to be slightly smaller than H_p. We do not consider this difference further here, other than to note that Levy and Zhang have suggested that the difference could result from different magnetic behaviors of bulk and interface Co atoms.[21]

An issue that we have not yet addressed in print is the possibility that the superconducting Nb leads above and below the CPP part of the sample might change the field on this part of the sample due to flux expulsion from the Nb. If the two Nb films and the sample multilayer were infinitely wide, flat planes, then the induced surface currents that eliminate the applied field within the Nb, would produce zero net field outside the Nb, thereby leaving only the applied field to act on the sample. Since our experiments show little differences in H_p or in variations with H for the CPP and CIP parts of our samples, we infer from experiment that field end effects in our "short-wide" geometry are small. However, we have not yet been able to derive the corrections for field end effects corresponding to those derived for current end effects in the Appendix.

There are also two problems in directly comparing the CIP- and CPP-MRs for our samples.

(1) The CIP and CPP parts of the sample are not sputtered onto the same material. The CPP part is sputtered onto 300 or 500 nm thick Nb layers, whereas the CIP part is sputtered directly onto the substrate. At 4.2 K, such thick Nb would superconduct and short out the CIP part. If the sample were raised to above the Nb superconducting temperature, the Nb layer would carry a significant fraction of the CIP current, since its thickness (300–500 nm) is comparable to that of a typical multilayer (720 nm). We show elsewhere[14] that, overall, the results for different situations are similar, CIP-MRs at H_o for CPP/CIP samples sputtered onto sapphire average a bit larger than those for single films sputtered onto silicon or 20–40 nm thick Nb, but those at H_p average a bit smaller.

(2) Our use of superconducting Nb contacts to ensure a uniform current in the CPP portion of the sample also introduces another complication. As detailed in Secs. IV and V, the Nb/Co (superconductor/ferromagnet) interfaces on both sides of the sample contribute terms to the CPP resistance. These extra resistances cancel out of the numerator of Eq. (1), but remain in the denominator, thereby reducing the measured CPP-MR from what it would be for the multilayer alone. The reduction is usually only several percent, but exceeds 100% in the largest case, where we have only two Co layers and one Ag layer. We present both our MR data and the ratio π=CPP-MR/CIP-MR as measured, and indicate only the largest corrections in Fig. 10(c) below. Complete data are given elsewhere.[14]

Lastly, we note that the CPP and CIP resistances at H_p and H_s, and the resulting values of MR(H_p), are all stable over time; on three different samples they either stayed the same [e.g., MR(H_p)=39% and 39%] or changed by only a few percent of their initial values [e.g., from MR(H_p)=52% to 50%] upon remeasuring after more than a year in air.

III. COMPARISON OF CPP- AND CIP-MRs

The samples described in this paper all have t_{Ag} and t_{Co} both $\geq$1.5 nm to ensure continuous layers,[19] and most of the samples have $t_{Ag}\geq$6 nm to minimize exchange coupling between the Co layers. Unfortunately, this range of layer thicknesses does not overlap with those in CIP-MR studies of Co/Ag multilayers published by others.[22] We, thus, have no independent comparisons for either our CPP or CIP data.

We present CPP- and CIP-MR measurements for seven series of multilayers. (1) Fixed Co thickness, t_{Co}, and variable Ag thickness, t_{Ag} with (a) t_{Co}=6 nm and fixed total thickness, t_T=720 nm; (b) t_{Co}=2 nm and fixed t_T=720 nm; and (c) t_{Co}=6 nm and fixed bilayer number N=60. (2) Fixed t_{Ag}=6 nm and variable t_{Co} with (a) fixed t_T=720 nm; and (b) fixed N=60. (3) t_{Ag}=t_{Co} with (a) fixed t_T=720 nm; and (b) fixed t_{Ag}=t_{Co}=6 nm and variable N. Full details are given Ref. 14.

(A) CPP-MR and CIP-MR. We look first at how our MRs vary with t_{Ag} for fixed t_{Co}. Figure 6(a) shows how CPP-MR(H_o) and CIP-MR(H_o) vary for both t_{Co}=6 nm and 2 nm [cases 1(a), 1(b), 1(c)]. Figure 6(b) shows the related variations of CPP-MR(H_p) and CIP-MR(H_p). We see that (a) the CPP-MR is always systematically larger than the CIP-MR; (b) as t_{Ag} increases, the MRs first rise, pass through a peak, and then gradually decrease, with more rapid decreases for cases 1(a) and 1(c) than for 1(b); and (c) for t_{Co}=6 nm, the peak occurs at a larger value of t_{Ag} for H_p than for H_o. The initial rise in MR with increasing t_{Ag} is probably due to a decrease in ferromagnetic coupling between Co layers, but it is not clear whether this decrease is due to a reduction of "pinholes" with increasing t_{Ag}, or to another cause. The slower falloff in the CPP- and CIP-MRs beyond the peak is more complex. For the CPP-MR, it is due in cases 1(a) and 1(b) to a more rapid fall in the numerator of Eq. (1) than in the denominator, and in case 1(c) to a slower increase in the numerator than in the denominator. The physics underlying these behaviors in the CPP-MR will be discussed in Secs. IV
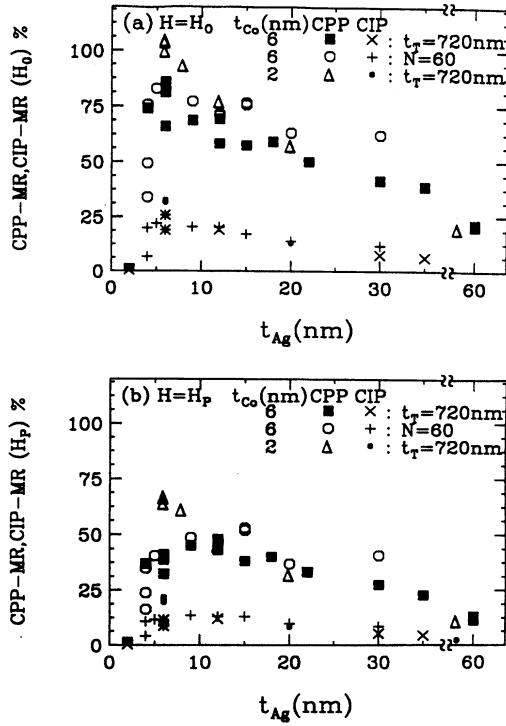
FIG. 6. CPP-MR ($\blacksquare$,$\bigcirc$,$\triangle$) and CIP-MR ($\times$,+,$\bullet$) vs t_{Ag} at H_o (a) and H_p (b) for a series of Co/Ag multilayers with fixed t_{Co}: ($\blacksquare$,$\times$) $t_{Co}=6$ nm and $t_T=720$ nm; ($\bigcirc$,+) $t_{Co}=6$ nm and $N=60$; and ($\triangle$,$\bullet$) $t_{Co}=2$ nm and $t_T=720$ nm.

FIG. 7. CPP-MR ($\bullet$,$\bigcirc$) and CIP-MR ($\times$,+) vs t_{Co} at H_o (a) and H_p (b) for a series of Co/Ag multilayers with fixed t_{Ag}: ($\bullet$,$\times$), $t_{Ag}=6$ nm and $t_T=720$ nm; ($\bigcirc$,+), $t_{Ag}=6$ nm and $N=60$.

and V. For the CIP-MR, the falloff in all three cases [1(a)–1(c)] is due mainly to decreasing ability of the electrons to sample Co layers as t_{Ag} increases.[2,7] Lastly, the reason why for $t_{Co}=6$ nm the MR peaks at a smaller value of t_{Ag} for H_o than it does for H_p is not yet known.

We examine next how the same quantities as in Figs. 6(a) and 6(b) vary with t_{Co} for fixed t_{Ag}. Here, Figs. 7(a) and 7(b) show that the MRs decrease monotonically with increasing t_{Co} with, again, the CPP-MR always larger than the equivalent CIP-MR. For both the CPP-MR and the CIP-MR, the increase in the denominators with increasing t_{Co} simply wins out over any bulk Co induced increases in the numerator. We will see in Sec. V that, for large t_{Co}, the decreases in the CPP-MR are even faster than expected from these two sources alone, suggesting that some other mechanism is also operating.

Lastly, we examine how the same quantities as in Figs. 7(a) and 7(b) vary with t_{Ag} or N when we hold $t_{Ag}=t_{Co}$. Figure 8 shows the data vs t_{Ag} for samples with fixed $t_T=720$ nm, and Fig. 9 shows the data vs N for these same samples and for ones with fixed $t_{Ag}=t_{Co}=6$ nm and variable t_T. In both figures, the MR increases with increasing number of Co/Ag interfaces, demonstrating that the interface contribution to the MR is very important. Again, the CPP-MR is always several times larger than the CIP-MR.

(B) π=CPP-MR/CIP-MR.[23] To examine the relationship between the CPP- and CIP-MRs quantitatively, we plot in Fig. 10 their ratio π=CPP-MR/CIP-MR versus t_{Ag}, t_{Co}, and N for the data of Figs. 6–9, respectively. As in Figs. 6–9, the
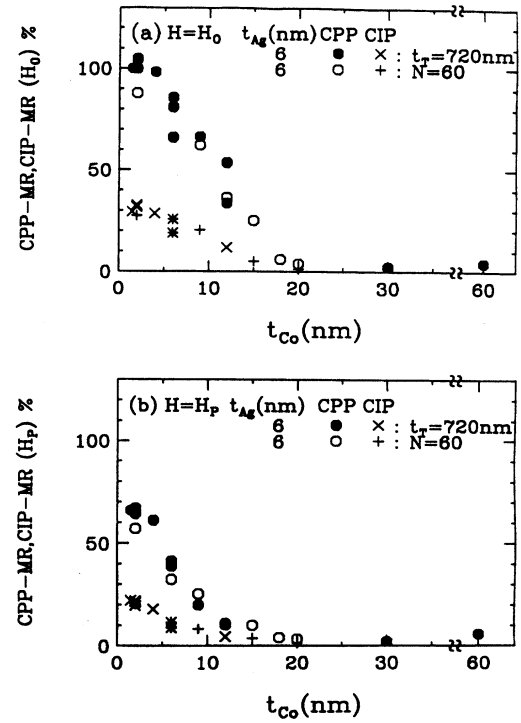
data in Fig. 10 are not corrected for the resistances of the two Nb/Co interfaces noted above, except for examples of some of the largest changes due to corrections (diamonds) in Fig. 10(c). We see from Fig. 10 that the uncorrected π increases from about 4 to 6 as t_{Ag} increases with t_{Co} held fixed, but remains nearly constant at 3 (to within experimental uncertainty) as t_{Co} increases with t_{Ag} held fixed. For $t_{Co}=t_{Ag}=6$ nm and variable N, the uncorrected π stays nearly constant, but the corrected π initially decreases rapidly with increasing N. Unfortunately, we cannot say much about the variation of π with increasing $t_{Co}=t_{Ag}$ for fixed t_T, because the CIP-MR data are not reliable for large $t_{Co}=t_{Ag}$.

IV. THE TWO CURRENT MODEL

We divide the conduction electrons in the multilayer into two classes, spin up (+) and spin down (−) relative to an arbitrary axis that, for simplicity, we take to be the axis of the applied field. Two assumptions underly the two-current model that we use in this paper:

(1) (+) and (−) electrons carry current through the sample independently. The work of Fert and Campbell[24] tells us that this assumption requires the spin-mixing length in F, l_{sm}, over which the currents mix, to be much longer than the mean-free-path in F. As spin-mixing is due mainly to electron-magnon scattering, this condition should hold at our measuring temperature of 4.2 K.[8,25]

(2) The spin directions, (+) or (−), are maintained as the electrons traverse the multilayer. Valet and Fert[8] pointed out that this maintenance requires two characteristic lengths, the
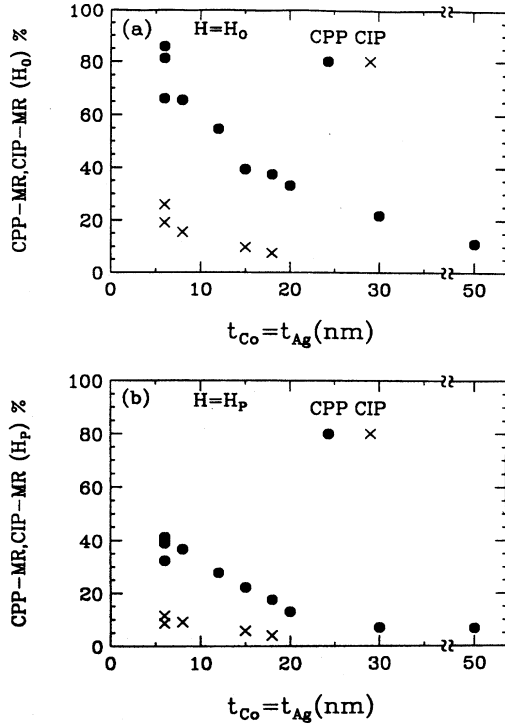
FIG. 8. CPP-MR (●) and CIP-MR (×) vs $t_{Co}=t_{Ag}$ at H_o (a) and H_p (b) for $t_T=720$ nm.
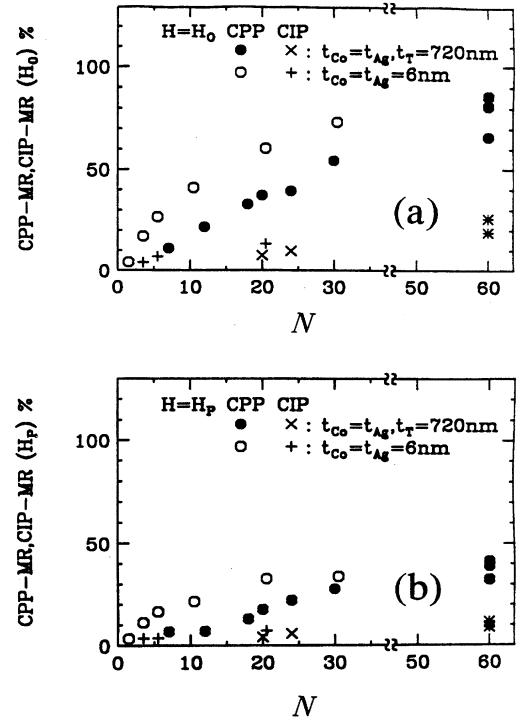

FIG. 9. CPP-MR (●,○) and CIP-MR (×,+) vs N at H_o (a) and H_p (b) for: (●,×), $t_{Co}=t_{Ag}$ with $t_T=720$ nm, and (○,+), $t_{Co}=t_{Ag}=6$ nm.

spin diffusion lengths l_{sf}^{Ag} and l_{sf}^{Co}, to be much longer than t_{Ag} and t_{Co}, respectively, and the probability of spin flips at the F/N interface must also be small. Assumptions (1) and (2) are not the same. In particular, l_{sf} and l_{sm} are dominated by different scattering processes. l_{sm} occurs only in the F layers and is dominated by electron-magnon scattering. l_{sf} is affected by all spin-flip processes in either the F or N layers: spin-orbit scattering, exchange scattering by paramagnetic impurities in the N layers, and (at high temperatures) electron-magnon scattering in the F layers.[25] There is good evidence that l_{sf}^N is quite long at 4.2 K in nonmagnetic metals such as Ag (Refs. 8, 26, and 27) when they do not contain impurities that flip spins.[27] l_{sf}^F in ferromagnetic metals such as Co should also be long because it is dominated by spin-orbit scattering.[8,25] The probability of spin flips at a sharp Co/Ag interface is likely small, but might become significant if the Ag and Co form a paramagnetic alloy. Fortunately, Co and Ag have very small mutual solubilities.[11]

When conditions (1) and (2) are satisfied, AR_t for electrons of spin direction (+) or (−) has been shown to be "self-averaging,"[6,28] i.e., the total scattering probability for an electron of a given spin direction that passes though the multilayer is simply the sum of the average scattering probabilities in the individual layers and at the interfaces. The usual mean-free paths for momentum transfer that appear in the resistivity, λ_p^{Co} and λ_p^{Ag}, drop out of the problem, and AR_t for a given spin direction is simply the series sum[6-8] of the appropriate resistivities times layer thicknesses, $\rho_i t_i$, of the materials comprising the multilayer, plus the ARs for all of the interfaces in the multilayer, independent of the ratios t_{Co}/λ_p^{Co} and t_{Ag}/λ_p^{Ag}. One then obtains expressions for the

CPP-AR_ts [Eqs. (2) and (3)] that are simple and give direct access to the fundamental physical parameters.

We are especially interested in AR_t in two specific magnetic states.

(A) Parallel (P) alignment of all of the local layer magnetizations, $\mathcal{M}_i$; of the Co layers. This alignment can be achieved simply by raising the applied magnetic field H to above the saturation field H_s at which all of the layers align, giving the saturation magnetization, $\mathcal{M}_s$.

(B) Antiparallel (AP) alignment of the $\mathcal{M}_i$, giving total magnetization $\mathcal{M}_T=0$. Here, the situation is more complex. In a variety of multilayers, coupling between the F layers oscillates from ferromagnetic (f) to antiferromagnetic (af) with decreasing coupling strength as t_N increases.[29] To avoid any systematic changes in coupling with changes in t_{Ag} or t_{Co}, we limit our analysis to samples with $t_{Ag} \geqslant 6$ nm, where the data on oscillatory MR for a variety of metals indicate that the F layers should be "uncoupled."[29,30] We showed in Sec. III that the CPP-MR then varies monotonically with t_{Ag} or t_{Co}.

If each Co layer is a single magnetic domain, with an $\mathcal{M}_i$ that can point only along or opposite to the applied magnetic field, then Zhang and Levy have argued[31] that the condition of total magnetization $\mathcal{M}=0$ should uniquely determine the CPP-AR_t^{AP}. Our data, however, do not show any such agreement at the two fields where $\mathcal{M} \approx 0$, H_o for the as-prepared sample, and H_p near the coercive field H_c after cycling to above H_s. Rather, as shown in Fig. 5 and elsewhere,[20] AR_t for our uncoupled samples ($t_{Ag} \geqslant 6$ nm) is systematically larger at H_o than at H_p. We must thus conclude that (a) our
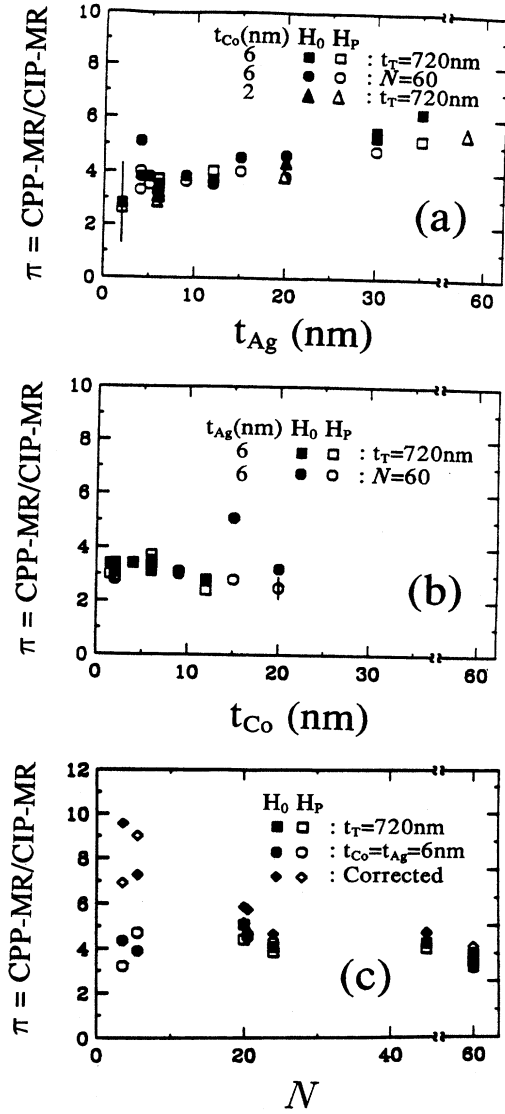
FIG. 10. (a) π=CPP-MR/CIP-MR vs t_{Ag} at H_o (filled symbols) and H_p (open symbols) for fixed t_{Co}=6 nm with ($\square$) t_T=720 nm and ($\bigcirc$) N=60, and for t_{Co}=2 nm with ($\triangle$) t_T=720 nm. (b) π=CPP-MR/CIP-MR vs t_{Co} at H_o (filled symbols) and H_p (open symbols) for fixed t_{Ag}=6 nm and ($\square$) t_T=720 nm and ($\bigcirc$) N=60. (c) π=CPP-MR/CIP-MR vs N at H_o (filled symbols) and H_p (open symbols) for t_{Ag}=t_{Co}, with ($\square$) t_T=720 nm and ($\bigcirc$) t_{Ag}=t_{Co}=6 nm. The diamonds ($\Diamond$) represent the data after correction by subtracting $2AR_{Co/Ag}$=6 fΩ m^2 from the denominator of the CPP-MR (see text).

Co layers are not single domain, and (b) that the condition $\mathcal{M}_b$≈0 does not uniquely specify AR_t in our samples.

For Co/Cu multilayers with t_{Co}=1.5 nm, the Co layers are known to have strong af coupling when t_{Cu}≈0.9 nm.[29] By combining the measured AR_t for this value of t_{Cu}, with extrapolation of Eq. (2) below to its independently determined limit at t_{Cu}=t_T, we showed that,[12] for uncoupled Co/Cu samples, $AR_t(H_o)$ lies close to AR_t^{AP}. Since Co/Ag does not show similarly strong af coupling, we have not been able to

make such a direct proof that $AR_t(H_o)$≈AR_t^{AP} for uncoupled Co/Ag samples. We have only indirect evidence of such near equality, in that values of $AR_t(H_o)$ for uncoupled Co/Ag multilayers[7,12] are quite similar to those for uncoupled Co/Cu multilayers with the same layer thicknesses.[12] Thus, strictly, for Co/Ag we must simply try H_o and examine the outcome. We have argued explicitly elsewhere[20] that $AR_t(H_o)$ for uncoupled Co/Ag samples is certainly a better estimate for AR_t^{AP} than is $AR_t(H_p)$. But, for completeness, and for comparison with data from other groups, we also include in the present paper data for $AR_t(H_p)$. As for the CPP-MRs in Sec. III, the data for $AR_t(H_p)$ behave qualitatively similarly to those for $AR_t(H_o)$, and yield parameters that are mostly only modestly different (Table I). More complete H_p data are given elsewhere.[14]

With this background, we now turn to the phenomenological equations to be tested, which we derived,[7] but which were presaged by the work of Zhang and Levy[6] (see also Edwards, Mathon, and Bechara Muniz[32]).

We take the Ag layer resistivities to be spin independent, $\rho_{Ag}^{\uparrow}$=$\rho_{Ag}^{\downarrow}$=$2\rho_{Ag}$, and assume that the resistivity of an electron passing through a Co layer, and the Co/Ag interface specific resistance, are both determined only by whether the electron spin is along or opposite to the local layer magnetization $\mathcal{M}_i$. Using the notation of Valet and Fert,[8] we write $\rho_{Co}^{\uparrow}$ ($\rho_{Co}^{\downarrow}$) and $R_{Co/Ag}^{\uparrow}$ ($R_{Co/Ag}^{\downarrow}$) for spin along (opposite to) $\mathcal{M}_i$, and define the parameters of interest by: $\rho_{Co}^{\uparrow}$=$2\rho_{Co}^{*}(1-\beta)$=$2\rho_{Co}/(1+\beta)$, $\rho_{Co}^{\downarrow}$=$2\rho_{Co}^{*}(1+\beta)$=$2\rho_{Co}/(1-\beta)$ and, similarly, $R_{Co/Ag}^{\uparrow\downarrow}$=$2R_{Co/Ag}^{*}(1\mp\gamma)$=$2R_{Co/Ag}/(1\pm\gamma)$. Here $AR_{Co/Ag}$ defines the magnitude of the Co/Ag interface resistance, and the "bulk" and "interface" anisotropy parameters β and γ are related to the more standard spin dependent anisotropy parameters,[33] α_F=$\rho_F^{\downarrow}/\rho_F^{\uparrow}$=$(1+\beta)/(1-\beta)$ and $\alpha_{F/N}$=$R_{F/N}^{\downarrow}/R_{F/N}^{\uparrow}$=$(1+\gamma)/(1-\gamma)$. Lastly, we account for the interface resistances between our Nb and Co layers, by including $R_{Nb/Co}^{\uparrow}$=$R_{Nb/Co}^{\downarrow}$=$2R_{Nb/Co}$ in each current channel.[34,35] For our Co/Ag multilayers, AR_t^{AP} and AR_t^{P} should then be given by

$$AR_t^{AP}=2AR_{Nb/Co}+(N-1)\rho_{Ag}t_{Ag}+N\rho_{Co}^{*}t_{Co}$$
$$+2(N-1)AR_{Co/Ag}, \qquad (2)$$

$$AR_t^{P}=AR_t^{AP}-[N\beta_{Co}\rho_{Co}^{*}t_{Co}$$
$$+2(N-1)\gamma_{Co/Ag}AR_{Co/Ag}^{*}]^2/AR_t^{AP}. \qquad (3a)$$

Here the $N-1$ terms result from assuming that the last Ag layer becomes superconducting by the proximity effect of its contact with Nb. When a Co capping layer is used, the $N-1$ multiplying ρ_N becomes N, the N multiplying ρ_F^{*} becomes $N+1$, and the $2(N-1)$ multiplying $AR_{F/N}^{*}$ becomes $2N$. Such differences are usually of minor importance for Co/Ag, as $\rho_{Ag}t_{Ag}$, $\rho_{Co}^{*}t_{Co}$, and $2AR_{Co/Ag}^{*}$ are all comparable to our measuring uncertainties. Rearranging Eq. 3(a) gives

$$\sqrt{[AR_t^{AP}-AR_t^{P}]AR_t^{AP}}=N\beta_{Co}\rho_{Co}^{*}t_{Co}$$
$$+2(N-1)\gamma_{Co/Ag}AR_{Co/Ag}^{*}. \qquad (3b)$$

TABLE I. Two-current model parameters for H_o (columns 2, 3) and for H_p (column 4). Column 1 contains the three parameters that can be independently measured. Column 2 contains parameters previously derived from three sets of data, assuming the listed independent measurement for $2AR_{Nb/Co}$.

	Independent measurements	H_o (3 sets)	H_o (4 sets)	H_p (4 sets)
$2AR_{Nb/Co}$ (fΩ m^2)	6 ± 1		6.9 ± 0.6	7.3 ± 0.6
ρ_{Ag} (nΩ m)	10 ± 1	10 ± 3	7.3 ± 1.9	10.9 ± 1.9
ρ_{Co} (nΩ m)	68 ± 10	82 ± 13	77 ± 12	77 ± 34
ρ_{Co}^* (nΩ m)		107 ± 10	100 ± 6	84 ± 6
β_{Co}		0.48 ± 0.05	0.48 ± 0.06	0.29 ± 0.06
α_{Co}		2.9 ± 0.4	2.9 ± 0.4	1.8 ± 0.4
$AR_{Co/Ag}^*$ (fΩ m^2)		0.56 ± 0.03	0.60 ± 0.02	0.45 ± 0.02
$AR_{Co/Ag}$ (fΩ m^2)		0.16 ± 0.04	0.18 ± 0.02	0.15 ± 0.02
$\gamma_{Co/Ag}$		0.85 ± 0.03	0.84 ± 0.04	0.82 ± 0.05
$\alpha_{Co/Ag}$		12_{-2}^{+5}	11.5_{-2}^{+4}	10_{-2}^{+4}

For fixed t_{Co}, Eq. 3(b) predicts that a plot of the *measured* left-hand side (LHS) versus $N-1$ should give a straight line passing closely through the origin (for $t_{Co}=6$ nm, the offset $\beta_{Co}\rho_{Co}^*t_{Co}\sim0.3$ fΩ m^2 is less than our measuring uncertainty), with slope independent of both ρ_{Ag} and t_T. We have shown that this slope is essentially the same for multilayers of both Co/Ag ($\rho_{Ag}\approx10$ nΩ m) and Co/AgSn ($\rho_{AgSn}\approx190$ nΩ m) with fixed $t_{Co}=6$ nm and $t_T=720$ nm,[7,12] and also for Co/Ag with fixed $t_{Co}=t_{Ag}=6$ nm and t_T varying from 18 to 720 nm.[34] These two Co/Ag data sets are included below.

We note that, if the Nb leads were eliminated, the first term in Eq. (2) would disappear, but both forms of Eq. (3) would be *unchanged*, i.e., Eqs. (3a) and (3b) retain the same form, whether or not the term $2AR_{Nb/Co}$ is included in Eq. (2). We will use this fact in our analysis in Sec. V.

Equations (2) and (3) contain six parameters, four in Eq. (2), $2AR_{Nb/Co}$, ρ_{Ag}, $\rho_{Co}^*=\rho_{Co}/(1-\beta^2)$, and $AR_{Co/Ag}^* = (AR_{Co/Ag})/(1-\gamma^2)$, and two more in Eqs. (3a) or (3b), β_{Co}, and $\gamma_{Co/Ag}$. Of these, three can, in principle, be independently measured: $2AR_{Nb/Co}$ using a series of sputtered Nb/Co/Nb sandwiches with varying Co thickness,[36] and ρ_{Ag} and ρ_{Co} on sputtered thin films.[7] The results of such independent measurements, and their estimated uncertainties, are listed in column 1 of Table I.

V. DATA AND ANALYSIS

A. Fit to four already published data sets

As discussed above, to minimize coupling between the Co layers, we limit our fits to multilayers with $t_{Ag}\geq6$ nm. To avoid situations where the hysteresis curves have shown additional structure beyond that in a simple multilayer,[14] we also limit the fits to $t_{Co}\leq18$ nm.

To compare data for ranges of t_{Ag} and t_{Co} with any simple model for AR_t, requires that the physical structure of the multilayers (which determines the Ag and Co resistivities ρ_{Ag} and ρ_{Co}, and the Co/Ag specific interface resistance $AR_{Co/Ag}$) and the magnetic structures of the Co layers both be independent of t_{Ag} and t_{Co}. We know, however, that our multilayers grow in columns beyond the first few layers, and that such growth can lead to increasing structural (including interfacial) disorder with increasing total sample thickness,

t_T.[18,37] Also, at 4.2 K, the resistivities of pure bulk Ag and Co are negligible compared to what we measure for sputtered thin Ag and Co films or infer about the Ag and Co layers in our multilayers. The film or layer resistivities must thus be determined by defects (grain boundaries, dislocations, etc.), the nature and concentration of which may change with t_{Ag} and t_{Co}. The magnetic structure of the Co layers might also change with t_{Co} because, among other reasons, Co can change its physical structure with increasing thickness, from the fcc structure of Ag for very thin Co layers, to the bulk Co hcp structure for very thick ones. For all these reasons, when we began our studies, it was not clear that even a correct simple two current model would accurately describe multilayers over wide ranges of t_{Ag}, t_{Co}, and total thickness, t_T, using fixed parameters for Co, Ag, and the interfaces.

In our previously published analyses of Co/Ag data,[7,34] we used three sample sets with fixed $t_T=720$ nm, (a) $t_{Co}=6$ nm, (b) $t_{Co}=2$ nm, and (c) $t_{Ag}=t_{Co}\leq18$ nm, and assumed the independently measured value of $AR_{Nb/Co}=6.1\pm1$ fΩ m^2. The values thus derived for ρ_{Ag}, ρ_{Co}^*, β_{Co}, $AR_{Co/Ag}^*$, and $\gamma_{Co/Ag}$ are given in column 2 of Table I.

In the present analysis, we add a fourth set, (d) fixed $t_{Ag}=t_{Co}=6$ nm with variable t_T, also add a few data points taken since the previous publications, and then calculate all six parameters with a two-part "global fitting" procedure based upon Ref. 38 and described in detail in Ref. 14.

The first part involves least-square minimization of χ^2 for a set of four linear equations derived by applying Eq. (2) to the four sets of data. As an example, we write out Eq. (2) explicitly for case (a), fixed $t_{Co}=6$ nm and fixed $t_T=720$ nm.

$$AR_t^{AP}=2AR_{Nb/Co}+[(N-1)/N]\rho_{Ag}t_T+\rho_{Co}^*t_{Co}+(N-1)$$

$$\times[(\rho_{Co}^*-\rho_{Ag})t_{Co}+2AR_{Co/Ag}^*]. \qquad (4)$$

With both t_{Co} and t_T constant, Eq. (4) predicts a linear variation of AR_t^{AP} with $N-1$, with an extrapolated ordinate intercept that is independent of the magnetic layer except for the extra term $\rho_{Co}^*t_{Co}\sim0.7$ fΩ m^2, which is smaller than our experimental uncertainty. Both the H_o and H_p data of Fig. 11(a) are consistent with straight lines extrapolated to the ordinate axis close to the expected value of
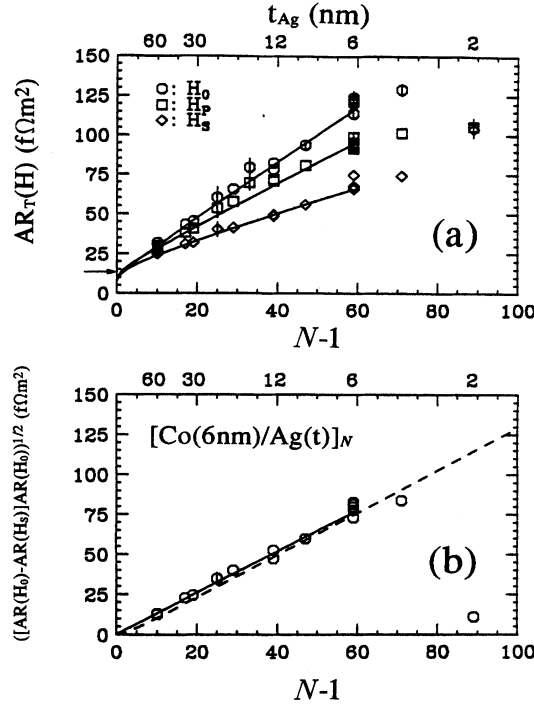
FIG. 11. (a) $AR_t(H)$ vs $N-1$ for H_o, H_p, and H_s for samples with $t_{Co}=6$ nm and $t_T=720$ nm. (b) $\sqrt{[AR_t(H_o)-AR_t(H_s)]AR_t(H_o)}$ vs $N-1$. The solid lines are fits with the parameters in columns 3 or 4 of Table I. The dashed curve is calculated from the VF theory for $l_{sf}^{Ag}=100$ nm and $l_{sf}^{Co}=\infty$.

$2AR_{Nb/Co}+\rho_{Ag}t_T\approx13$ fΩ m^2 (arrow) obtained from the independently measured quantities in column 1 of Table I. The downturn in the curves in Fig. 11(a) at small N is due to the $(N-1)/N$ factor multiplying $\rho_{Ag}t_T$.

These four linear equations are solved for the four parameters of Eq. (1). The results of H_o are given in in column 3 of Table I, and the equivalent results for H_p are given in column 4. The fits for the AP states are shown in Figs. 11(a)–14(a) as solid lines for both H_o and H_p. Importantly, the values of $2AR_{Nb/Co}$ and ρ_{Ag} derived for both H_o and H_p agree with the independently measured ones in column 1 to within mutual uncertainties, and the new values of ρ_{Co}^* and $AR_{Co/Ag}^*$ for H_o also agree with those in column 2. Lastly, the values of ρ_{Co}^* and $AR_{Co/Ag}^*$ for H_p are only about 20% less than those for H_o.

The second part of the analysis involves least-squares minimization of χ^2 to find β_{Co} and $\gamma_{Co/Ag}$ from either Eqs. (3a) or (3b). Again we write out explicitly the equations for case (a):

$$AR_t^P=AR_t^{AP}-[N\beta_{Co}\rho_{Co}^*t_{Co}+2(N$$
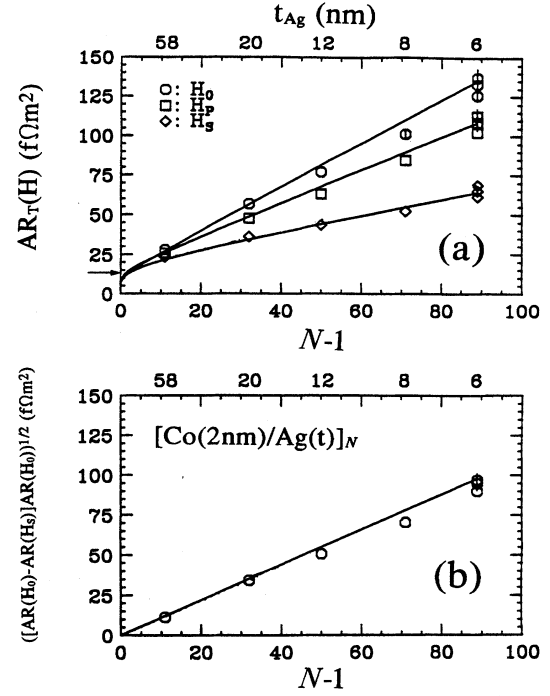$$-1)\gamma_{Co/Ag}AR_{Co/Ag}^*]^2/AR_t^{AP} \qquad (5a)$$

and

FIG. 12. (a) $AR_t(H)$ vs $N-1$ for H_o, H_p, and H_s for samples with $t_{Co}=2$ nm and $t_T=720$ nm (b) $\sqrt{[AR_t(H_o)-AR_t(H_s)]AR_t(H_o)}$ vs $N-1$. The solid lines are fits with the parameters in columns 3 or 4 of Table I.

$$\sqrt{[AR_t^{AP}-AR_t^P]AR_t^{AP}}$$
$$=(N-1)[\beta_{Co}\rho_{Co}^*t_{Co}+2\gamma_{Co/Ag}AR_{Co/Ag}^*]+\beta_{Co}\rho_{Co}^*t_{Co}.$$
$$(5b)$$

From Eq. (4), we see that AR_t^{AP} is linear in $N-1$ for large N, but becomes nearly constant for small N. This behavior causes the AR_t^P of Eq. 5(a) to deviate from linearity in $N-1$, thereby explaining the curvature at low $N-1$ of the H_s data of Fig. 11(a) needed to reach the same intercept at $N-1=0$ as that for AR_t^{AP}. Equation (5b) predicts that a plot of the square root LHS versus $N-1$ should give a straight line passing very close to the origin, a prediction consistent with the data of Fig. 11(b).

To test the sensitivity of β_{Co} and $\gamma_{Co/Ag}$ to fitting procedure, we used two alternatives to calculate these two quantities, assuming the values already determined for ρ_{Co}^* and $AR_{Co/Ag}^*$.

(A) Fit the appropriate form of Eq. (3b) [e.g., (5b)] using the experimental data for both AR_t^P and AR_t^{AP}. The values for this fit, our preferred one, are given in column 3 of Table I for H_o and column 4 for H_p. The resulting curves for the H_s data in Figs. 11(a)–14(a) and for the square-root data of Figs. 11(b)–14(b) are shown as solid lines similar to those for H_o and H_p. These curves agree with the data of Figs. 11–13 to well within their uncertainties. The arrows on the ordinate axes of Figs. 11–13 are the extrapolated intercepts predicted for AR_t^{AP} with no adjustability from the indepen-
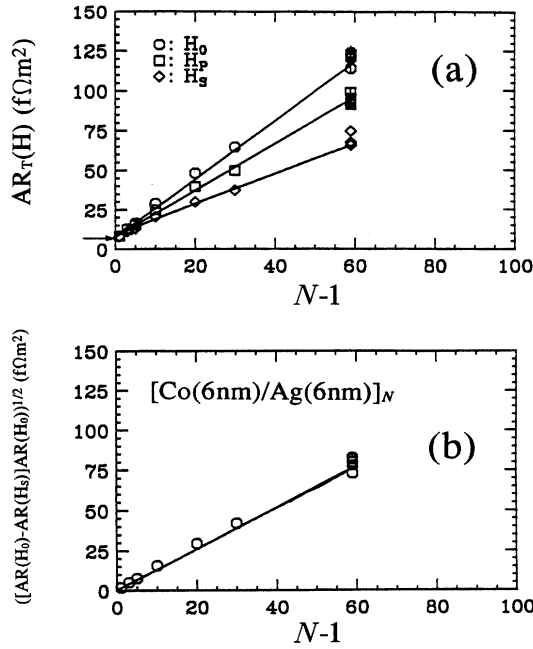
FIG. 13. (a) $AR_t(H)$ vs $N-1$ for H_o, H_p, and H_s for samples with $t_{Co}=t_{Ag}=6$ nm. (b) $\sqrt{[AR_t(H_o)-AR_t(H_s)]AR_t(H_o)}$ vs $N-1$. The solid lines are fits with the parameters in columns 3 or 4 of Table I.

dently measured values of $AR_{Nb/Co}$ and ρ_{Ag} given in column 1 of Table I. In all three cases the data are compatible with these predictions. For Fig. 14, the curves also agree to within mutual uncertainties with those data for $t_{Ag}=t_{Co}\leqslant 18$ nm ($N-1\geqslant 19$) that were included in the fits. However, the curves lie at the upper end of the uncertainties for the thickest of these layers and clearly lie above the data for still thicker layers.

(B) Fit the appropriate form of Eq. (3a) using the experimental data for AR_t^P, but values for AR_t^{AP} calculated from the fit to the appropriate form of Eq. (2). The values from this fit, given elsewhere,[14] agree with those in column 3 of Table I to within their mutual uncertainties.

In the fits to the H_o and H_p data, the number of degrees of freedom are the number of data points (36) less the number of parameters (4), giving 32. The derived values of χ^2 were ~225, indicating that the deviations of the data from the fits are not determined solely by measuring uncertainties. We presume that the deviations are due not to failure of the equations, but rather to small, uncontrolled, changes in sample physical and magnetic structures in different sputtering runs, or as t_{Ag} and t_{Co} change. Based upon this assumption, we determine the uncertainty for each parameter given in Table I by multiplying the uncertainty from the least-squares minimization by the square root of the ratio of χ^2 to the degrees of freedom, $\sqrt{225/32}\approx 2.7$. We examine correlations between β and γ elsewhere.[14]

Since the new global fit to the four sets of combined H_o and square root data gives values of the parameters $2AR_{Nb/Co}$, ρ_{Ag}, and ρ_{Co}, consistent with those independently measured, and values of the parameters $AR_{Co/Ag}^*$, β_{Co}, and $\gamma_{Co/Ag}$ consistent with those we previously derived using a
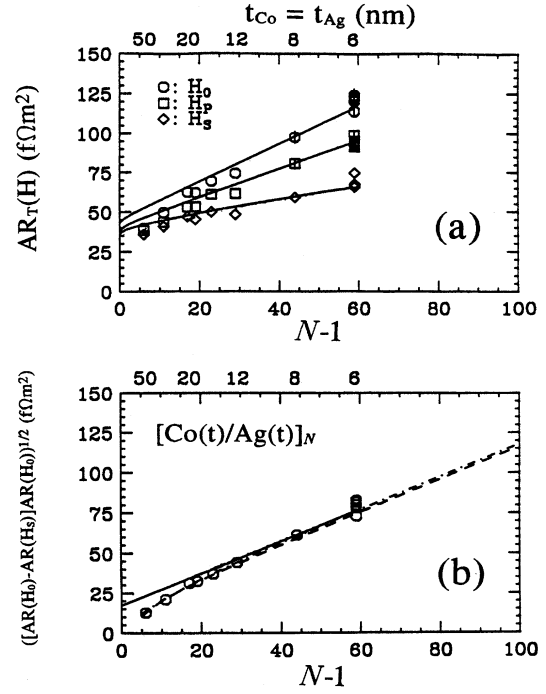

FIG. 14. (a) $AR_t(H)$ vs $N-1$ for H_o, H_p, and H_s for samples with $t_{Co}=t_{Ag}$ and $t_T=720$ nm. (b) $\sqrt{[AR_t(H_o)-AR_t(H_s)]AR_t(H_o)}$ vs $N-1$. The solid lines are fits with the parameters in columns 3 or 4 of Table I. The dashed and broken curves are calculated from the VF theory for $l_{sf}^{Ag}=100$ nm and $l_{sf}^{Co}=6$ nm, respectively, with the other taken as infinite.

subset of the same data (column 2), we conclude that these parameters provide a meaningful representation of the four data sets for our Co/Ag samples. The question of the stability of β_{Co}, $\gamma_{Co/Ag}$, and $AR_{Co/Ag}^*$ under more general preparation conditions requires further study.

B. Predictions of the behavior of new data sets

With the success of the previous section in hand, we ask next how well the parameters in columns 3 and 4 of Table I can describe data taken on three additional sets of samples, one with t_{Co} and N held fixed and t_{Ag} varied, and two with t_{Ag} held fixed and t_{Co} varied.

We consider first the samples with variable t_{Ag}. For these samples, Eq. (2) predicts that AR_t^{AP} should increase with increasing t_{Ag}, due only to the term $\rho_{Ag}t_{Ag}$, and the square root on the LHS of Eq. (3b) should be constant. Data on samples prepared along with the others in this paper are shown as open symbols in Fig. 15, and the predictions of the parameters in columns 3 are again shown as solid lines. The data can be viewed in two ways: (a) as consistent with predictions, to within uncertainties, for $t_{Ag}\leqslant 15$ nm, but then falling below for larger t_{Ag}, or (b) as simply having the wrong slopes, negative for $AR_t(H_o)$ and the square root and nearly zero for $AR_t(H_p)$ and $AR_t(H_s)$, instead of positive for all three $AR_t s$ and zero for the square root. Since the disagreements between the data and predictions hinge upon a single datum for $t_{Ag}=30$ nm, we recently sputtered a new set
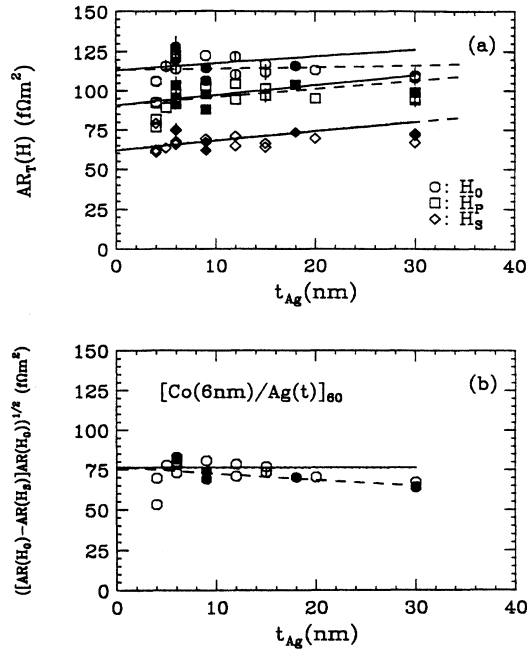
FIG. 15. (a) $AR_t(H)$ vs $N-1$ for H_o, H_p, and H_s for samples with $t_{Co}=6$ nm and $N=60$. (b) $\sqrt{[AR_t(H_o)-AR_t(H_s)]AR_t(H_o)}$ vs $N-1$. The solid lines are fits with the parameters in columns 3 or 4 of Table I. The dashed curves in (a) are calculated from an approximation to the VF theory for $l_{sf}^{Ag}=100$ nm and $l_{sf}^{Co}=\infty$ (see text). The dashed curve in (b) is calculated from the VF theory for $l_{sf}^{Ag}=100$ nm and $l_{sf}^{Co}=\infty$. The open symbols designate samples made along with the others in this study. The filled symbols designate samples made more recently (see text).

of samples, including two with $t_{Ag}=30$ nm, this time with a 6 nm Co capping layer to kill any proximity effect between the top Ag layer and the covering Nb strip. To within internal variations in each set, the new data (filled symbols), agree with the old ones (the corrections for the capping layer are <1 fΩ m^2). The new data confirm a clear deviation from prediction for $t_{Ag}=30$ nm, but slightly strengthen the case for consistency with predictions for $t_{Ag}\leqslant20$ nm. Two obvious potential sources of the deviations for $t_{Ag}=30$ nm are (a) a finite value of l_{sf}^{Ag}, and (b) changes in structural properties of the Ag and Co with increasing t_{Ag} that change ρ_{Ag}, ρ_{Co}, and $AR^*_{Co/Ag}$. We consider these alternatives below, after examining data for variable t_{Co}.

Figure 16 shows the data and predictions for fixed $t_T=720$ nm, and Fig. 17 shows them for fixed $t_{Ag}=6$ nm and $N=60$. The H_s data are all consistent with prediction, except for the $t_{Co}=60$ nm point in Fig. 16, which suggests some structural change in that sample. In contrast, the H_o, H_p, and square root data fall increasingly below the predictions as t_{Co} increases beyond 9 nm (in Fig. 16, where $N-1$ decreases below 50). In addition to the possible sources for deviations listed for the data of Fig. 15, except with l_{sf}^{Ag} replaced by l_{sf}^{Co}, there is now also the possibility of changes in magnetic properties with changing t_{Co}, such as increased coupling as the Co layers thicken. We briefly examine these possibilities, particularly that l_{sf}^{Ag} and l_{sf}^{Co} could be finite.
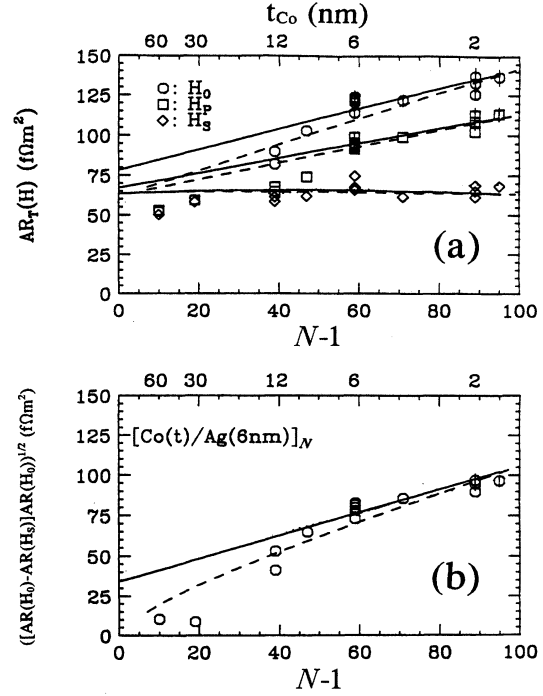

FIG. 16. (a) $AR_t(H)$ vs $N-1$ for H_o, H_p, and H_s for samples with $t_{Ag}=6$ nm and $t_T=720$ nm. (b) $\sqrt{[AR_t(H_o)-AR_t(H_s)]AR_t(H_o)}$ vs $N-1$. The solid lines are fits with the parameters in columns 3 or 4 of Table I. The dashed curves in (a) are calculated from an approximation to the VF theory for $l_{sf}^{Co}=0.5$ nm and $l_{sf}^{Ag}=\infty$. The dashed curve in (b) is calculated from the VF theory for $l_{sf}^{Co}=0.5$ nm and $l_{sf}^{Ag}=\infty$.

C. Examination of effects of finite l_{sf}^{Ag} and l_{sf}^{Co}

To study effects of finite l_{sf}^{Ag} and l_{sf}^{Co}, we must use generalizations of Eqs. (2) and (3) by Valet and Fert (VF).[8] Because their equations are complex, we limit ourselves to graphical analysis. For two reasons, this analysis is only semiquantitative. First, the VF equations result from a lowest-order analysis that is valid only when $l_{sf}^{Ag}\gg\lambda_p^{Ag}$ and $l_{sf}^{Co}\gg\lambda_p^{Co}$ For our multilayers, $\lambda_p^{Ag}\sim80-100$ nm and $\lambda_p^{Co}\sim10-40$ nm,[39] and we will see that potentially interesting values of l_{sf}^{Ag} or l_{sf}^{Co} are less than or equal to these values. A quantitative comparison must thus await extension of the VF analysis to higher order. Second, the VF equations have not yet been rigorously generalized to samples with superconducting Nb contacts. Since, as noted in the discussion after Eq. (3), Eq. (3b) is the same with or without Nb contacts, we approximate the effect on Eq. (3b) of reducing l_{sf}^{Ag} and l_{sf}^{Co} by using the VF equations directly.[8,27] For Eqs. (2) and (3a), in contrast, we must correct for the Nb contacts. There, we use an ad-hoc procedure developed by one of us[35] that reduces to Eqs. (2) and (3a) with Nb contacts in the limit l_{sf}^{Ag} and l_{sf}^{Co} $=\infty$, and approximates the VF equations elsewhere.

The VF predictions for the square root functions of the samples of Fig. 11, fixed $t_{Co}=6$ nm and Fig. 14, $t_{Co}=t_{Ag}$, are shown in Figs. 18 and 19, respectively, as dotted curves for reduced l_{sf}^{Ag} and dashed curves for reduced l_{sf}^{Co}. In both figures the predictions are clearly much more sensitive to l_{sf}^{Ag}
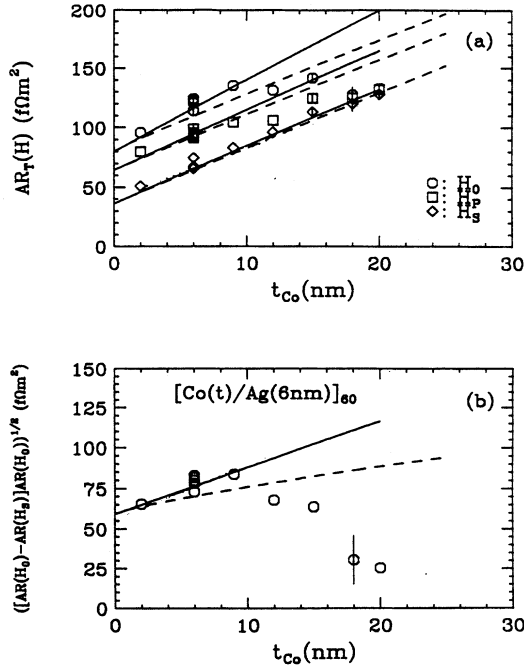
FIG. 17. (a) $AR_t(H)$ vs t_{Co} for H_o, H_p, and H_s for samples with $t_{Ag}=6$ nm and $N=60$. (b) $\sqrt{[AR_t(H_o)-AR_t(H_s)]AR_t(H_o)}$ vs $N-1$. The solid lines are fits A with the parameters in columns 3 or 4 of Table I. The dashed curves in (a) are calculated from an approximation to the VF theory for $l_{sf}^{Co}=0.5$ nm and $l_{sf}^{Ag}=\infty$. The dashed curve in (b) is calculated from the VF theory for $l_{sf}^{Co}=0.5$ nm and $l_{sf}^{Ag}=\infty$.
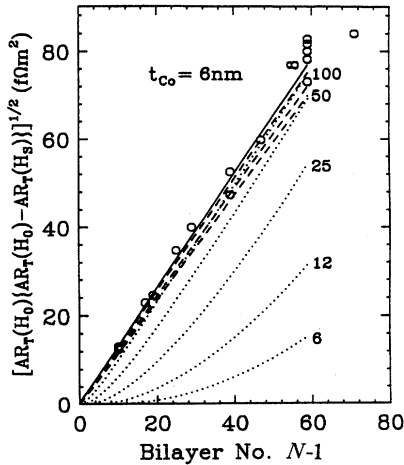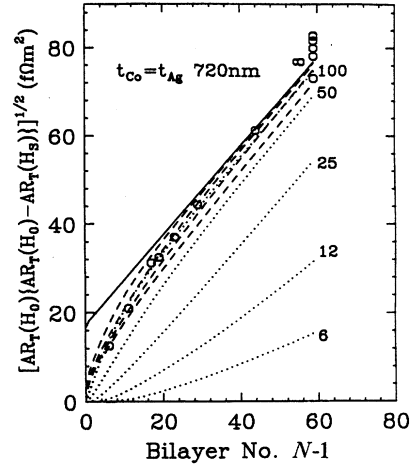

FIG. 19. $\sqrt{[AR_t(H_o)-AR_t(H_s)]AR_t(H_o)}$ vs $N-1$ for the data of Fig. 14. The solid line is calculated from Eq. (2b) ($l_{sf}^{Ag}=l_{sf}^{Co}=\infty$) with the parameters of column 3 of Table I. The dotted curves are calculated from the VF theory for the indicated values of l_{sf}^{Ag}, with $l_{sf}^{Co}=\infty$. The dashed curves are calculated from the VF theory for (top to bottom) $l_{sf}^{Co}=12$, 6, 3, and 0 nm with $l_{sf}^{Ag}=\infty$.

than to l_{sf}^{Co}. In Fig. 18 (data of Fig. 11), the solid straight line for $l_{sf}^{Ag}=l_{sf}^{Co}=\infty$ gives the best fit, showing that the data are consistent with very long l_{sf}^{Ag} and l_{sf}^{Co}. Similar behavior was found also for the data of Figs. 12 and 13. In Fig. 19 (data of Fig. 14), in contrast, better fits are found with either $l_{sf}^{Ag} \sim 100$ nm or $l_{sf}^{Co} \sim 6$ nm. We thus have two possibilities: (a) that $l_{sf}^{Ag} \sim 100$ nm and/or $l_{sf}^{Co} \sim 6$ nm, and the parameters of Table I have to be modified to fit the data of Fig. 18 with such values; or (b) that l_{sf}^{Ag} and l_{sf}^{Co} are both much longer than these values, and the deviations of the data of Fig. 18 from the solid line have other causes. Based upon our previous estimate of $l_{sf}^{Ag} \sim 500$ nm,[27] and the expectation that l_{sf}^{Co} should be much longer than 6 nm,[25] we favor alternative (b). But to test the two alternatives further, we now examine whether $l_{sf}^{Ag} \sim 100$ nm and/or $l_{sf}^{Co} \sim 6$ nm can explain the deviations from predictions found in Figs. 15–17.

Figure 15 shows that most of the deviations of the H_o, H_p, and square root data from the straight lines for $l_{sf}^{Ag}=\infty$ can be described by $l_{sf}^{Ag}=100$ nm, leaving only a modest residual to be explained by structural changes. For H_s, however, $l_{sf}^{Ag}=100$ nm gives almost no change from $l_{sf}^{Ag}=\infty$, and almost all of the observed deviations must be attributed to structural changes. Combining these results, we see that some structural changes must be included in a complete description of the data. And, as noted above, some structural changes are inevitable, since our sputtered samples, like most others,[18,37] grow in columns with widths that increase somewhat with layer thickness. As direct evidence for some changes, Table II shows that H_p increases systematically with increasing t_{Ag}, a behavior that requires changes in the properties of at least the Co layers (or in their coupling) with t_{Ag}. Further studies are needed to see if changes in the resistivities of the Co and Ag layers alone are large enough to explain the behavior of our data.

FIG. 18. $\sqrt{[AR_t(H_o)-AR_t(H_s)]AR_t(H_o)}$ vs $N-1$ for the data of Fig. 11. The solid line is calculated from Eq. (2b) ($l_{sf}^{Ag}=l_{sf}^{Co}=\infty$) with the parameters of column 3 of Table I. The dotted curves are calculated from the VF theory for the indicated values of l_{sf}^{Ag}, with $l_{sf}^{Co}=\infty$. The broken lines are calculated from the VF theory for values of $l_{sf}^{Co}=3$ nm (top), 1 nm (middle), and 0 nm (bottom), with $l_{sf}^{Ag}=\infty$.

TABLE II. H_p-CPP (rounded to nearest 5 Oe) vs t_{Ag} for samples with fixed $t_{Co}=6$ nm and $N=60$. Old samples (open symbols in Fig. 15) were sputtered at the same time as most of the others in this paper. New ones (filled symbols in Fig. 15) were sputtered more recently.

t_{Ag} (nm)	H_p (Oe) (old)	H_p (Oe) (new)
6	75–110[a]	85
9	90	95,105
12	95,115	
15	120,155	
18		145
20	180	
30	185	165,195

[a]Six values ranged from 75 to 110 and averaged 90.

Turning now to Figs. 16 and 17, we find that even reducing l_{sf}^{Co} to 0.5 nm (Ref. 40) is not enough to describe the data for H_o, H_p, and the square root. While the VF, analysis breaks down for such small values of $l_{sf}^{Co}(\ll \lambda_p^{Co})$, it seems unlikely that it will do so in just the way needed to fit the data. Rather, the deviations are much more likely due to structural or magnetic changes. Since we do not see how structural changes alone could so strongly affect $AR_t(H_o)$ and $AR_t(H_p)$, and yet so little affect $AR_t(H_s)$, which is very nearly as expected for $l_{sf}^{Co}=\infty$, we infer that the deviations of the data from predictions in Figs. 16 and 17 arise from increased ferromagnetic coupling between Co layers as t_{Co} increases but t_{Ag} is held fixed. Such coupling might arise from increasing Co layer roughness or increasing number of "pinholes." The magnetization curves do not show any direct evidence of such increased coupling, but these curves look very similar [see Fig. 5(c)] for all $t_{Co}<20$ nm, and may well be dominated by the behaviors of the individual layers. These samples need to be studied by techniques that could reveal any increased coupling. We conclude by noting that increased coupling of Co layers with increasing t_{Co} could also explain why the $AR_t(H_o)$ and $AR_t(H_p)$ data in Fig. 14 fall below the predicted straight lines as $N\rightarrow 0$. The fact that t_{Ag} is increasing also, provides a natural explanation for why the deviations from predictions in Fig. 14 are smaller than those in Figs. 16 and 17, where t_{Ag} is held fixed.

VI. SUMMARY AND CONCLUSIONS

In Sec. II, we described how we make Co/Ag multilayer samples for simultaneous CPP-MR and CIP-MR measurements, focusing upon a masking system. In Sec. III we reported two important sets of results on Co/Ag multilayers with wide ranges of Co and Ag layer thicknesses. (1) We found the variations of the CPP- and CIP-MRs with t_{Ag} and t_{Co} to be qualitatively similar to each other. These similarities suggest that the parameters that control the CPP- and CIP-MRs are also likely to be similar. (2) At both H_o and H_p, we always found CPP-MR>CIP-MR, with their ratio π ranging from 3 to 6. This behavior strongly supports theoretical predictions of $\pi>1$.[6,9]

In Sec. IV, we outlined the two-current, series resistor model to be used in analyzing our CPP-AR data quantitatively, noting the assumptions underlying the model and its

limitations, the most important of which is that it assumes very long spin-diffusion lengths ($l_{sf}^{Ag},l_{sf}^{Co}\gg t_{Ag},t_{Co}$). In Sec. V we examined the ability of this model to describe data on a wide variety of Co/Ag multilayers, using data for both H_o and H_p. We find that the six parameters obtained by fitting the model to the data of Figs. 11–14 at H_o and H_s (or H_p and H_s) agree to within mutual uncertainties both with the five parameters obtained from earlier fits to the data of Figs. 11, 12, and 14 alone, and with the three found from independent measurements. The curves then obtained from these parameters describe the data of Figs. 11–13 very well, with no need for corrections for any changes in structural properties (i.e., in ρ_{Ag}, ρ_{Co}, or $AR_{Co/Ag}$) with changing t_{Co} or t_{Ag}. The curves also describe reasonably well those data of Fig. 14 used in the fit, i.e., $t_{Co}=t_{Ag}\leq 18$ nm. For thicker Co and Ag layers, however, significant deviations of the data from the curves require for their explanation either smaller values of l_{sf}^{Ag} and l_{sf}^{Co} (i.e., $l_{sf}^{Ag}\sim 100$ nm or $l_{sf}^{Co}\sim 6$ nm), or else changes in physical or magnetic structures with increasing $t_{Co}=t_{Ag}$. Independent evidence suggests that such small values of l_{sf}^{Ag} and l_{sf}^{Co} are unlikely, placing the burden mainly on structural changes. The data of Fig. 15 also deviate from the predicted curves. These deviations can be explained either by a combination of $l_{sf}^{Ag}\approx 100$ nm plus modest structural changes with changing t_{Co}, t_{Ag}, or by a larger l_{sf}^{Ag} and larger structural changes. Lastly, the data of Figs. 16 and 17 deviate most strongly from predictions and cannot be explained even by reducing l_{sf}^{Co} to nearly zero. Those deviations must be due to increased ferromagnetic coupling between Co layers as t_{Co} increases, a mechanism that could also explain the smaller deviations from prediction of the data of Fig. 14. However, independent evidence of such increased coupling remains to be obtained. We conclude that we now understand much about the CPP-MRs of Co/Ag multilayers, but that further studies of effects of changes in structural and magnetic properties are needed to understand them completely.

APPENDIX: ANALYSIS OF "NONIDEALITIES" IN OUR CROSSED-STRIP GEOMETRY (FIG. 1)

1. Edge and corner effects

Consider two long, thin superconducting strips of width W that are "crossed" on opposite sides of a slab of thickness t, lateral extent $2R$, and conductivity σ, Fig. 20(a). The potential difference between the strips is V and the total current flowing between them is I. For our samples, $W\approx 1.1$ mm, $R\sim 2W$, and $t\approx 0.7$ μm. A perspective view of this geometry is shown in Fig. 20(b), where the slab is omitted for clarity and the dashed lines indicate the boundary of the overlap
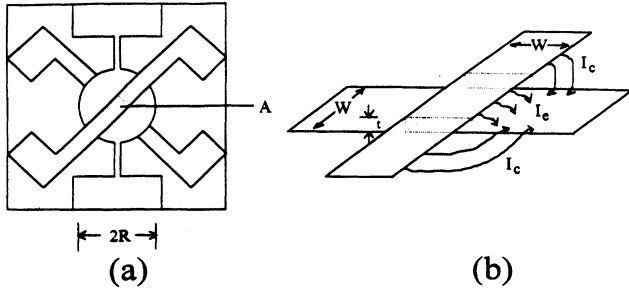
FIG. 20. Top (a) and perspective (b) view of crossed-strip geometry.

region $W \times W$. The "edge" (I_e) and "corner" (I_c) fringing currents are shown for one side of the top strip.

Summary of mathematical results

Edge currents: I_e flows from near an edge of one strip to the opposite strip. These currents are significant only within $\approx t$ of the $W \times W$ boundary. With four edges, $I_e = (VW^2 \sigma/t) 4\alpha(t/W)$, where $\alpha = \ln(4)/\pi = 0.44$, see (a), below.

Corner currents: I_c flows between the corner-shared extended edges (beyond $W \times W$), as shown. The E field will vary as $= 1/r$, where r is the radial distance from a corner. Since at the four corners the shortest distance between the strips is t, we integrate from $r = t$ to $r = R$, and obtain $I_c = (VW^2 \sigma/t) 4\beta(t/W)^2 \ln(R/t)$, where $\beta = (2/\pi) = 0.64$, see section (b) below.

The total current should thus be

$$I = (W^2 V \sigma/t)[1 + 4\alpha(t/W) + 4\beta(t/W)^2 \ln(R/t)$$
$$+ \text{higher order}], \qquad (A1)$$

and in terms of the correct AR(CPP), we obtain

$$AR(\text{CPP}) = (t/\sigma)$$
$$= [W^2 V/I][1 + 4\alpha(t/W)$$
$$+ 4\beta(t/W)^2 \ln(R/t) + \text{higher order}],$$
$$(A2)$$

with $t/W \approx 0.6 \times 10^{-3}$, AR(CPP) differs from $(W^2 V/I)$ by $\approx 0.1\%$.

(a) Evaluate α for I_e: In Fig. 21(a), the $y = t$ and $y = 0$ planes contain the upper and lower strips of Fig. 20, respectively. The third conductor in the $y = 2t$ plane is a mathematical device included to satisfy the boundary conditions imposed by the slab having a free surface in the plane of the
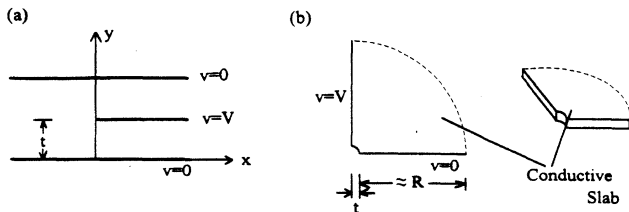

FIG. 21. (a) Approximate geometry for evaluating α for I_e. (b) Approximate geometry for evaluating β for I_c.
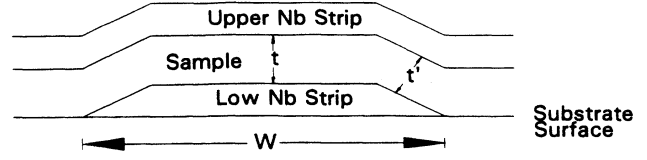

FIG. 22. Schematic of a sample with Nb strip profiles such as that shown in Fig. 4 in the text.

upper strip in Fig. 20. In Fig. 21(a), the whole region between $y = 0$ and $y = 2t$ is filled with material of conductivity σ. The problem is solved by the conformal map $x + iy = \ln[\cosh(u + iv)]$, where the lines of constant v in the x,y plane are equipotentials. Upon scaling we obtain the potential $\Phi = \text{Im}(2V/\pi)\text{arccosh}\{\exp[\pi(x + iy)/2t]\}$. Computing the vertical electric field at the lower conducting slab surface from: $E = \partial\Phi/\partial y|_{y=0}$, we find directly that $E(x) = (V/t)[e^{-2\xi} + 1]^{-1/2}$, where $\xi = (\pi x/2t)$. Integrating along the bottom plate in the above figure from $x = -\infty$ to $+W$, we find

$$I = W\sigma \int_{-\infty}^{0} E(x)dx + W\sigma \int_{0}^{R} [E(x) - V/t]dx. \quad (A3)$$

Note for Eq. (A3) that I is defined in terms of the deviation of $E(x)$ from the ideal case where $E(x) = 0$ for $-B < x < 0$ and $E(x) = V/t$ for $0 < x < W$. In the limit $e^{-R/t} \ll 1$, the upper limit of the second integration can be taken equal to ∞ and we obtain $\alpha = \ln(4)/\pi$.

(b) Evaluate β for I_c: Figure 21(b) shows how we approximate the three-dimensional (3D) problem for Fig. 20(b) by a 2D geometry, where the inner cutoff is t, the minimum distance between the two strip extensions in Fig. 20. We thus ignore the component of the field lines that is perpendicular to the slab. We use the conformal map $x + iy = e^{u + iv}$. Now the electric field falls off as $1/r$ from the center, which yields a logarithmic term: i.e., $E = (2/\pi)(V/r)$ gives

$$I = \sigma t \int_{t}^{R} E(r)dr = (\sigma t 2V/\pi)\ln(R/t),$$

so that $\beta = (2/\pi)$.

2. The lack of sharp Nb strip edges

Figure 4 in the text shows an actual surface profile for a Nb strip on one of our Co/Ag samples demonstrating that sputter deposition through a contact mask does not produce sharp edges. Since a sample of thickness t (≈ 0.7 mm) is deposited on top of such a strip, we ask: What are the consequences for AR(CPP) measurements of the strip edges not being sharp? In Fig. 4 the assigned width W of the strip is indicated by the two dotted lines. These dotted lines are positioned where the apparent thickness of the Nb is less than about 10 nm, a thickness below which independent experiments by us indicate that a Nb film in contact with Co is normal at 4.2 K. Based on three profile measurements of each strip, we usually determine W to an accuracy of $\approx \pm 2\%$. Thus in defining the area of the $W \times W$ region with nonsharp edges, our typical random uncertainties in A are= $\approx \pm 4\%$.

Do nonsharp edges cause significant systematic errors in AR_t(CPP)? In Fig. 22 we redraw (*not-to-scale*) Fig. 4 sche-

matically. The main question is how the true thickness of the sloping edges, t', compares to t. If shadowing was minimal, the thickness t' of the sample perpendicular to the sloping Nb/sample boundary would be less than t. In fact in the limit of a sharp edge (vertical slope), t' would approach zero,

causing a short between the two Nb strips. In Fig. 5, however, the maximum slope is only $\approx 0.5\%$, and the largest slope we have seen is only $\approx 1.5\%$. Thus the difference between t' and t is negligible and not having sharp edges is an advantage for this issue.

---

[*]Present address: Laboratoire de Physique des Solides, Batiment 510, Universite de Paris Sud, Orsay, France.

[†]Present address: Physics Department, AL al-Bayt University, Mafraq, Jordan.

[‡]Author to whom correspondence should be addressed.

[1]See, e.g., L. M. Falicov et al., J. Mater. Res. 5, 1299 (1990).

[2]M. N. Baibich et al., Phys. Rev. Lett. 61, 2472 (1988).

[3]See, e.g., G. Binash et al., Phys. Rev. B 39, 4828 (1989); C. Dupas et al., J. Appl. Phys. 63, 4300 (1988), S. S. P. Parkin, N. More, and K. P. Roche, Phys. Rev. Lett. 64, 2304 (1990); S. S. P. Parkin, R. Bhadra, and K. P. Roche, ibid. 66, 2152 (1991); D. H. Mosca et al., J. Magn. Magn. Mater. 93, 480 (1990); D. H. Mosca et al., ibid. 94, L1 (1991).

[4]W. P. Pratt, Jr. S.-F. Lee, J. M. Slaughter, R. Loloee, P. A. Schroeder, and J. Bass, Phys. Rev. Lett. 66, 3060 (1991).

[5]M. A. M. Gijs, S. K. J. Lenczowski, and J. B. Giesbers, Phys. Rev. Lett. 70, 3343 (1993); M. A. M. Gijs et al., Appl. Phys. Lett. 63, 111 (1993); S. K. J. Lenczowski et al., J. Appl. Phys. 75, 5154 (1994); M. A. M. Gijs et al., ibid. 75, 6709 (1994).

[6]S. Zhang and P. M. Levy, J. Appl. Phys. 69, 4786 (1991).

[7]S. F. Lee et al., J. Magn. Magn. Mater. 118, L1 (1993).

[8]T. Valet and A. Fert, Phys. Rev. B 48, 7099 (1993).

[9]See, e.g., P. M. Levy, in Solid State Physics Series, edited by H. Ehrenreich and D. Turnbull (Academic, New York, 1994), Vol. 47, p. 367; G. E. W. Bauer, Phys. Rev. Lett. 69, 1676 (1992); H. C. Camblong, S. Zhang, and P. M. Levy, Phys. Rev. B 47, 4735 (1993); Y. Asano, A. Oguri, and S. Maekawa, ibid. 48, 6192 (1993); H. Itoh, J. Inoue, and S. Maekawa, ibid. 51, 342 (1995).

[10]I. K. Schuller (unpublished).

[11]M. Hanson and K. Anderko, Constitution of Binary Alloys, Metallurgy and Metallurgical Engineering Series (McGraw-Hill, New York, 1958).

[12]P. A. Schroeder et al., in Magnetism and Structure in Systems of Reduced Dimension, edited by R. F. C. Farrow et al., NATO ASI Series (Plenum, New York, 1993), p. 129; P. A. Schroeder et al., in Magnetic Ultrathin Films: Multilayers and Surface/Interfaces and Characterization, edited by B. T. Janker et al., MRS Symposia Proceedings No. 313 (Materials Research Society, Pittsburgh, 1993), p. 47; W. P. Pratt et al., J. Magn. Magn. Mater. 126, 406 (1993); W. P. Pratt et al., J. Appl. Phys. 73, 5326 (1993); J. Bass et al., ibid. 75, 6699 (1994).

[13]J. M. Slaughter, W. P. Pratt Jr., and P. A. Schroeder, Rev. Sci. Instrum. 60, 127 (1989).

[14]S.-F. Lee Ph.D. thesis, Michigan State University, 1994.

[15]W. P. Pratt, Jr., C. Fierz, R. Stubi, and R. Loloee (unpublished).

[16]D. L. Edmunds, W. P. Pratt, Jr., and J. A. Rowlands, Rev. Sci. Instrum. 51, 1516 (1980).

[17]See, e.g., M. Tinkham, Superconductivity (Gordon and Breach, New York, 1965).

[18]P. Galtier et al., in Magnetic Ultrathin Films: Multilayers and Surface/Interfaces and Characterization (Ref. 12), p. 749; M. B. Stearns (unpublished); D. A. Howell and M. B. Crimp (unpublished).

[19]A. M. van Alphen, P. A. A. van der Heijden, and W. J. M. de Jonge. J. Appl. Phys. 76, 6607 (1994); E. A. M. van Alphen et al. (unpublished).

[20]P. A. Schroeder, S.-F. Lee, P. Holody, R. Loloee, Q. Yang, W. P. Pratt, Jr., and J. Bass, J. Appl. Phys. 76, 6610 (1994).

[21]P. M. Levy and S. Zhang (private communication).

[22]H. Sato et al., Superlatt. Microstruct. 4, 45 (1988); S. Araki, K. Yasui, and Y. Narumiya, J. Phys. Soc. Jpn. 60, 2827 (1991); S. Araki, J. App. Phys. 73, 3910 (1993); M. Tan, J. A. Barnard, M. R. Parker, and D. Selae, in Magnetic Ultrathin Films: Multilayers and Surface/Interfaces and Characterization (Ref. 12), p. 191; G. Tosin et al., J. Magn. Magn. Mater. 121, 399 (1993).

[23]The symbol π=CPP-MR/CIP-MR follows past practice in Refs. 4 and 6. The reader should be forewarned that this symbol and Π=MR(H_o)/MR(H_p) are interchanged in Ref. 14.

[24]A. Fert and I. A. Campbell, J. Phys. F 6, 849 (1976).

[25]A. Fert, J. L. Duvail, and T. Valet, Phys. Rev. B 52, 6513 (1995).

[26]M. Johnson, Phys. Rev. Lett. 70, 2142 (1993).

[27]Q. Yang, P. Holody, S.-F. Lee, L. L. Henry, R. Loloee, P. A. Schroeder, W. P. Pratt, Jr., and J. Bass, Phys. Rev. Lett. 72, 3274 (1994); J. Bass, Q. Yang, S. F. Lee, R. Loloee, P. A. Schroeder, and W. P. Pratt, Jr., J. Appl. Phys. 75, 6699 (1994).

[28]Camblong, S. Zhang, and P. M. Levy, J. Appl. Phys, 75, 6906 (1994); Phys. Rev. B 47, 4735 (1993).

[29]See, e.g., S. S. P. Parkin, N. More, and K. P. Roche, Phys. Rev. Lett. 64, 2304 (1990).

[30]P. A. Schroeder, P. Holody, S.-F. Lee, R. Loloee, W. P. Pratt, Jr., and J. Bass, in Magnetic Ultrathin Films: Multilayers and Surface/Interfaces and Characterization (Ref. 12), p. 47.

[31]S. Zhang and P. M. Levy, Phys. Rev. B 47, 6776 (1993).

[32]D. M. Edwards, J. Mathon, and R. Bechara Muniz, IEEE Trans. Magn. 27, 3548 (1991).

[33]See, e.g., A. Fert and I. A. Campbell, J. Phys. F. 6, 849 (1976); P. M. Levy, in Solid State Physics Series, edited by H. Ehrenreich and D. Turnbull (Academic, New York, 1994), Vol. 47, p. 367.

[34]W. P. Pratt, Jr., S.-F. Lee, P. Holody, Q. Yang, R. Loloee, J. Bass, and P. A. Schroeder, J. Magn. Magn. Mater. 126, 406 (1993); J. Bass, P. A. Schroeder, W. P. Pratt, Jr., S.-F. Lee, Q. Yang, P. Holody, L. L. Henry, and R. Loloee, Mater. Sci. Eng. B31, 77, 1995.

[35]W. P. Pratt, Jr. (unpublished).

[36]C. Fierz, S.-F. Lee, W. P. Pratt, Jr., P. A. Schroeder, and J. Bass, J. Phys. Condens. Matter. 2, 1224 (1991).

[37]A. E. M. De Veriman, F. J. G. Hakkens, and A. G. Dirks, Ultramicroscopy 51, 306 (1993).

[38]S. L. Meyer, Data Analysis for Scientists and Engineers (Wiley, New York, 1986).

[39]S.-F. Lee, W. P. Pratt, Jr., R. Loloee, P. A. Schroeder, and J. Bass, Phys. Rev. B 46, 548 (1992).

[40]We use $l_{sf}^{Co}=0.5$ nm for calculating $AR_t(H_o)$, $AR_t(H_p)$ and $AR_t(H_s)$ in Figs. 16 and 17 because our ad-hoc procedure diverges when l_{sf}^{Co} is much smaller than this value. The VF equations tell us that the curves for $l_{sf}^{Co}=0.5$ nm lie close to those for $l_{sf}^{Co}=0$.